Chapter 6
Nanostructured Metal Oxides for Supercapacitor Applications

Katlego Makgopa, Abdulhakeem Bello, Kumar Raju, Kwena D. Modibane, and Mpitloane J. Hato

Contents

Abstract The fundamental properties of supercapacitors (SCs) with descriptions restricted to the metal oxides systems and the effect on the electrochemical performance and synthesis are described in this chapter. Metal oxides such as manganese oxide (MnO), vanadium oxide (V_2O_5) and ruthenium oxide (RuO) have

K. Makgopa (✉)
Department of Chemistry, Faculty of Science, Tshwane University of Technology (Acardia Campus), Pretoria, South Africa
e-mail: makgopak@tut.ac.za

A. Bello
Department of Materials Science and Engineering, African University of Science and Technology (AUST), Abuja, Nigeria

K. Raju
Energy Materials, CSIR Materials Science and Manufacturing, Pretoria, South Africa

K. D. Modibane · M. J. Hato
Department of Chemistry, School of Physical and Mineral Sciences, University of Limpopo (Turfloop), Polokwane, South Africa

R. Saravanan et al. (eds.), *Emerging Nanostructured Materials for Energy and Environmental Science*, Environmental Chemistry for a Sustainable World 23,
https://doi.org/10.1007/978-3-030-04474-9_6

demonstrated great potential in the field of energy storage due to their structural as well as electrochemical properties, thus attracting huge attention in the past decade and in recent years. The major contributing factor to the electrochemical properties is their capability to achieve relatively high pseudocapacitive performance derived from their theoretical values resulting from their multiple valence state changes. The developments of the metal oxide (MO)-based electrode materials and their composites are being explored from the synthetic point of view as well as their emerging applications as energy storage materials. Therefore, the need to further exploration of MO-based electrodes is motivated by their considerably low-cost and environmentally friendly nature as compared to other supercapacitive electrode materials. This chapter accounts to the overview of various nanostructured metal oxide materials for application as energy storage materials in supercapacitors.

6.1 Introduction

Today's society and particularly the developing countries rely heavily on fossil fuels as the primary source of energy since they are cheap and also exhibits high specific energy and power per weight (or per volume) output. The growing world population and increasing standard of life-style exerted much pressure on the deliverance of energy, and as a result, these have led to a rapidly increasing energy demand over a period of time (Poizot and Dolhem 2011). In addition, the fast-growing interest in portable electronic devices and electric vehicles has stimulated extensive research in high-performance energy storage devices. The above reasons are justified by the projections stated in the *International Energy Outlook 2017* (IEO 2017 https://www.eia.gov/outlooks/ieo/) reference case, which shows that the total world energy consumption continues to rise from 575 quadrillion British thermal units (Btu) in 2015 to 736 quadrillion Btu in 2040, indicating an increase of 28% (IEA 2014). The incineration of fossil fuels results in severe environmental pollution and contributes to greenhouse effect, which is harmful to the environment while also placing many countries at disadvantage as the rate of coal depletion exceeds that of its production. The development of technology that is compatible with the resources provided by nature is essential in order to reduce the uprising malice to the environment by fossil fuel energy sources worldwide and also to meet the high energy demands resulting from the growth in civilization. Renewable energy has shown to be the escalating solution towards mitigating this energy crisis, and currently, they are the world's fastest-growing energy source, with consumption increasing by an average 2.3%/year between 2015 and 2040 (Bang et al. 2000; UNEP 2013). As much as renewable energy resources (i.e. photovoltaics, wind turbines, geothermal heat, etc.) have displayed great potential to be employed as the alternative energy sources to fossil fuels globally, their success is still limited by their inability to store the harvested energy and a lack of a quick transmission of the same energy (Hatzell et al. 2015).

Thus, the market for energy storage applications becomes an integrated critical component in clean energy development and sustainability. Electrochemical energy storage systems (EES) have emerged as an established, valuable approach for improving the reliability and overall use of the advantages of renewable energy resources (Béguin et al. 2014). An energy storage device is an apparatus used to store electrical energy when needed and releases the stored energy when required. The role of the technology involving energy storage device in the fields such as renewable energy generation and electric/hybrid electric automobile systems has become increasingly important in modern society as a measure of checking the ever-increasing global warming and other matters related to the energy crisis. Therefore, in consideration of reliable, stable and sustainable large-scale use of renewables, electrochemical capacitors (ECs) and batteries play a fundamental role in advanced and highly efficient energy storage and management. Lithium–ion batteries (LIBs) can store large amount of energy as high as 150–200 Wh kg^{-1} but are confined to their low-power density (below 1000 W kg^{-1}) and poor cycle life (usually less than 1000 cycles) (Thackeray et al. 2012; Béguin et al. 2014). In comparison with batteries, electrochemical capacitors (ECs) vastly known as supercapacitors have demonstrated to be the competing measures with regards to storing energy output that can be delivered at the faster rate without the loss of the device efficiency (Burke et al. 2014). This electrochemical energy storage device has great potential in energy applications that require peak power pulses. The ability of the ECs to serve as a gap between conventional capacitors (that display great power output but limited energy storage output) and batteries (with great energy storage output but limited power deliverance) places this electrochemical energy storage device at the much added advantage. The advantages of ECs arise from their energy storage mechanism, which involves physical storage of energy through dielectric polarization or electronic double layer of ions and electrons (surface phenomenon). There are two types of fundamental storage mechanisms involved in ECs, viz. (a) 'electrochemical double layer capacitor' (EDLC) that uses nanocarbons as the main electrode materials for supercapacitors, and there are many abundant sources of nanocarbons with facile processes for the fabrication of cheap electrodes (Ghosh and Lee 2012) and (b) 'pseudocapacitor'. The operation mechanism of the EDLC involves the non-faradaic separation of charges at the 'double layer (i.e. electrode/electrolyte interface), while pseudocapacitor involves fast faradaic, redox reaction of electroactive materials at the interface (Béguin et al. 2014). A Ragone chart in Fig. 6.1 shows the power and energy densities of various energy storage and conversion devices.

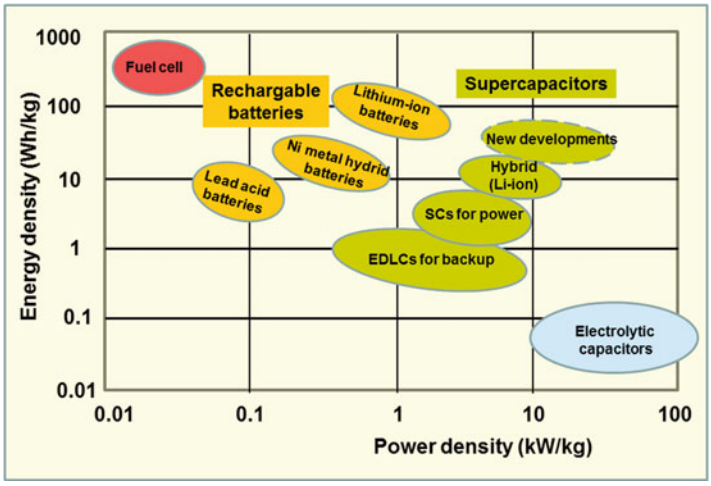

Fig. 6.1 Ragone chart showing energy density as a function of power density of various capacitors and batteries

6.1.1 Electrochemical Capacitors as an Energy Storage Solution

The concept of the electrochemical double-layer capacitance dates back to a German physicist, Hermann von Helmholtz, in 1853 (Conway 1999). In 1957, General Electric Company filed the earliest ECs patented based on the double-layer capacitance structure. However, not until the 1990s did EC technology begin to draw some attention in the field of hybrid electric vehicles (Burke 2000). It was found that the main function of ECs could promote the electrochemical performance of a battery or fuel cell in a hybrid electric vehicle by providing necessary power for acceleration and recuperating brake energy (Toupin et al. 2004). Thus, the capacitor technology is regarded as a promising means for storing electricity (Jiang et al. 2013). The early electrochemical capacitors (ECs) were rated at a few volts and had capacitance values measured from fractions of farads up to several farads. Today's trend is for cells with the size ranging from small millifarad-sized devices with exceptional pulse power performance up to devices rated at several kilo farads. The technology is experiencing increasingly broader use especially originating from the 'humble' beginning, both replacing batteries in some cases and in others complementing their performance (Miller and Burke 2008). Due to the intrinsic properties occurring at the electrode/electrolyte interface of an EC device, understanding of the materials used for fabricating the device is of great importance especially for the enhancement of the electrochemical performance of the EC device (Conway 1999; Béguin et al. 2009). Figure 6.2 shows the composition and working principle of an ideal parallel plate capacitor. In a charged capacitor, the metal plates are oppositely charged, and an electric field is formed in the dielectric medium (Thomas and Floyd 2009).

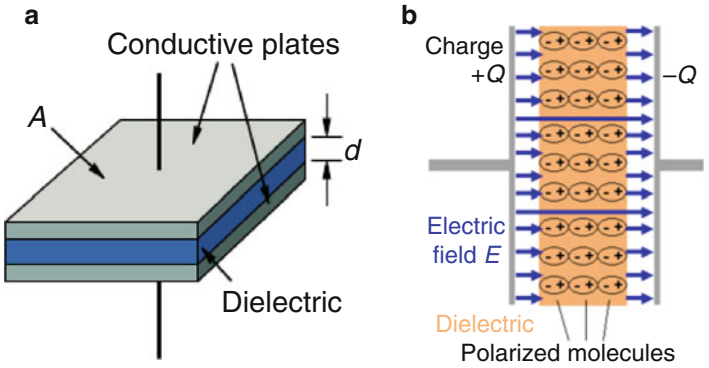

Fig. 6.2 Schematic diagrams of (**a**) the design of a parallel plate capacitor (with permission of Yuan et al. 2012) and (**b**) a charged parallel plate capacitor (With permission of Vol'fkovich et al. 2002)

Generally, to improve on the electrochemical performance of ECs, electroactive materials that provide supercapacitive effect contributing to the total double-layer capacitance are considered. Pseudocapacitance originates from electrochemical reduction-oxidation (Redox) reaction due to faradic transfer that occurs in the active electrode materials. This phenomenon is similar to the chemical reaction that occurs in many rechargeable batteries; therefore, the reaction must be reversible or quasi-reversible for optimum/efficient electrochemical performance. Taking into account a uniform distribution of the redox-based material on the electrodes, the redox process is governed by the reaction below (Yu et al. 2013a):

$$O_X + n_e^- X \leftrightarrow R_D \tag{6.1}$$

where n is the number of electrons transferred and O_X and R_D represent the oxidized and reduced species, respectively.

The electrochemical potential arising from Eq. 6.1 has been described by the Nernst equation:

$$E = E^0_{O_X/R_d} + \frac{\mathrm{RT}}{\mathrm{nF}} \ln\left(\frac{C_{O_X}}{C_{R_d}}\right) \tag{6.2}$$

The faradaic reaction in Eq. 6.1 corresponds to a reversible pseudocapacitance (per/vol) given by Eq. 6.3 for an ideal system.

$$C_{pc}(E) = \frac{idt}{dE} = \frac{i}{v} = \frac{n^2\mathrm{F}^2}{RT} dC^0_{O_x} \frac{\exp\left(\frac{n\mathrm{F}}{\mathrm{RT}}\left(E^0_{O_X/R_d} - E\right)\right)}{\left[1 + \exp\left(\frac{n\mathrm{F}}{\mathrm{RT}}\left(E^0_{O_X/R_d} - E\right)\right)\right]^2} \tag{6.3}$$

However, taking into account the irregularities in the matrix structure of the electrodes leads to uneven distribution of the redox centres and therefore leads to a quasi-reversible reaction and can be resolved by introducing a lateral interaction energy ($-g\frac{C_{O_X}}{C^0_{O_X}}$) term, and Eq. 6.3 can then be modified to Eq. 6.4 as shown below (Yu et al. 2013a).

$$C_{\mathrm{pc}}(E) = \frac{n^2F^2}{\mathrm{RT}}\mathrm{dC}^0_{O_x}\frac{\exp\left(\frac{nF}{RT}\left(E^0_{O_X/R_d}-E\right)+g\frac{C_{O_X}}{C^0_{O_X}}\right)}{\left[1+\exp\left(\frac{nF}{RT}\left(E^0_{O_X/R_d}-E\right)+g\frac{C_{O_X}}{C^0_{O_X}}\right)\right]^2+g\exp\left(\frac{\mathrm{nF}}{RT}\left(E^0_{O_X/R_d}-E\right)+g\frac{C_{O_X}}{C^0_{O_X}}\right)} \tag{6.4}$$

Equation 6.4 holds for a completely reversible redox reaction system when $g = 0$ and quasi-reversible reaction when $g > 0$. The capacitance defined by Eq. 6.4, which is a function of electrode potential, is known as the momentary capacitance. The intrinsic pseudocapacitance (C_{sp}, measured in F/g) of the redox reaction is expressed by Eq. 6.5:

$$C_{pc} = \frac{\mathrm{AM_{mw}}}{m}\sum_{j=1(E_{\mathrm{on}})}^{j=n(E_{\mathrm{off}})}C_{pc}(E_j) = \frac{n^2}{mRT}\frac{F^2}{}\mathrm{AdM_{mw}}C^0_{O_X}\frac{\exp\left(\frac{nF}{RT}\left(E^0_{O_X/R_d}-E\right)+g\frac{C_{O_X}}{C^0_{O_X}}\right)}{\left[1+\exp\left(\frac{nF}{RT}\left(E^0_{O_X/R_d}-E\right)+g\frac{C_{O_X}}{C^0_{O_X}}\right)\right]^2+g\exp\left(\frac{nF}{RT}\left(E^0_{O_X/R_d}-E\right)+g\frac{C_{O_X}}{C^0_{O_X}}\right)} \tag{6.5}$$

where A is the electrode geometric area (cm^2), d is the thickness of the electrode layer, M_{mw} is the molecule weight of the redox material (g), m is the weight of redox material inside the entire electrode layer (g) and E_{on} and E_{off} are the onset and offset potentials.

The incorporation or combination of electrodes having double layer and pseudocapacitance leads to a coupling effects between the two materials taking advantage of the synergy to enhance the total capacitance of the electrodes. Thus, for an ideal condition, the total capacitance (C_T) of an electrode must be the sum of electrochemical double-layer capacitance (C_{dl}) and pseudocapacitance (C_{pc}) which is expressed in Eq. 6.6:

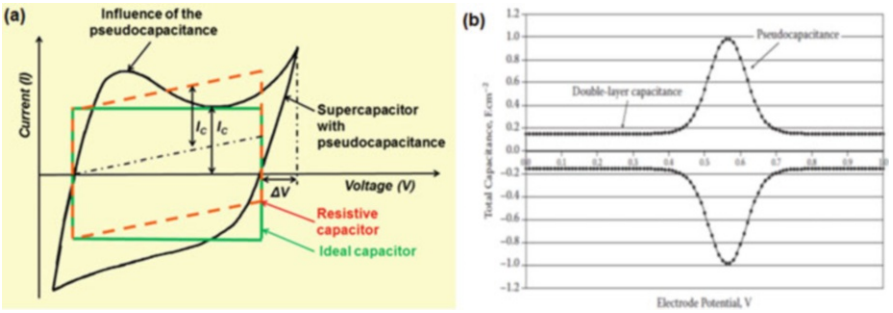

Fig. 6.3 (**a**) CV curves showing fundamental differences between static capacitance (rectangular) and pseudo-/faradaic capacitance (curved) and (**b**) shows the calculated total capacitance as a function of electrode potential reflecting the double-layer capacitance and the pseudocapacitance contribution (Yu et al. 2013a)

$$
\begin{aligned}
C_T &= C_{\mathrm{dl}} + C_{pc}(E) \\
&= C_{\mathrm{dl}} + \frac{n^2F^2}{\mathrm{RT}} dC^0_{O_X} \\
&\quad \times \frac{\exp\left(\frac{nF}{\mathrm{RT}}\left(E^0_{O_X/R_d} - E\right) + g\frac{C_{O_X}}{C^0_{O_X}}\right)}{\left[1 + \exp\left(\frac{nF}{\mathrm{RT}}\left(E^0_{O_X/R_d} - E\right) + g\frac{C_{O_X}}{C^0_{O_X}}\right)\right]^2 + g\exp\left(\frac{nF}{\mathrm{RT}}\left(E^0_{O_X/R_d} - E\right) + g\frac{C_{O_X}}{C^0_{O_X}}\right)}
\end{aligned}
\tag{6.6}
$$

Figure 6.3 is a reversible cyclic voltammetry of an electrode showing the total computed capacitance against the potential. This capacitance clearly shows the double-layer capacitance and the huge contribution from the pseudocapacitive components, indicating that materials that exhibit pseudocapacitance would significantly contribute to the development of supercapacitor technology.

Different faradaic mechanisms can occur in electrochemical charge storage in pseudocapacitors, and these include electrosorption (underpotential deposition), reduction-oxidation reactions (redox pseudocapacitance) and intercalation (intercalation pseudocapacitance). These processes are illustrated in Fig. 6.4 (Augustyn et al. 2013).

Underpotential deposition occurs when the onset of deposition of metal adatoms (adsorbed atom) at various types of substrates in potential ranges positive to the reversible equilibrium potential (also referred to as the Nernst potential). A classic example of underpotential deposition is the deposition of lead (Pb) on the surface of a gold (Au) electrode (Sudha and Sangaranarayanan 2002). While redox pseudocapacitance occurs when the electrochemical adsorption of ions near surface or onto the surface of a material with a concomitant faradaic charge transfer (Augustyn et al. 2014), e.g. surface redox reactions as in RuO_X (Augustyn et al. 2013). Intercalation pseudocapacitance occurs when ions intercalate into the pores or layers

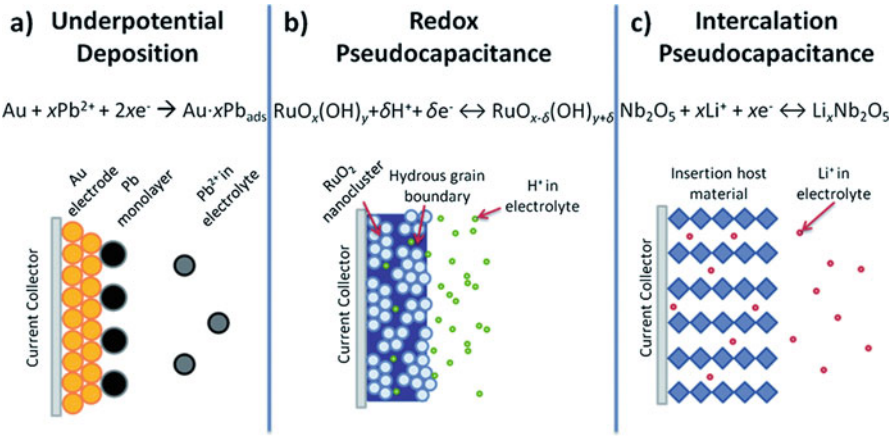

Fig. 6.4 Schematic showing different types of reversible redox mechanisms that give rise to pseudocapacitance (With permission of Augustyn et al. 2014)

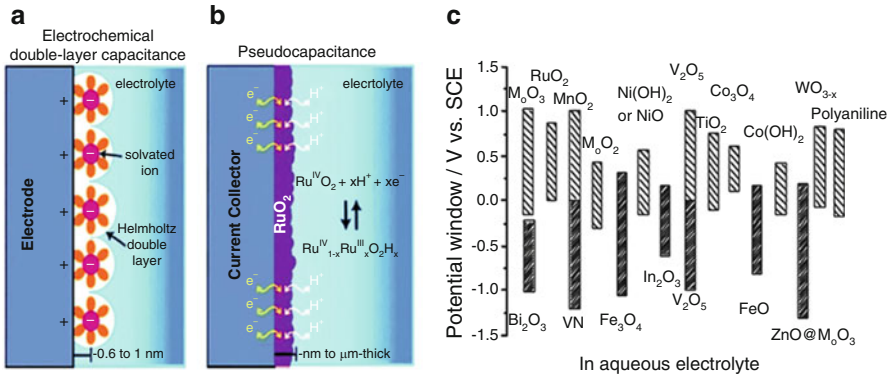

Fig. 6.5 Schematic representation of the mechanism in (**a**) double capacitors, (**b**) pseudocapacitors, (With permission of Zhang et al. (2016a) and (**c**) the working potential windows of various pseudocapacitve-type materials in aqueous electrolyte (With permission of Qu et al. 2011))

of a redox active material accompanied by a faradaic charge transfer with no crystallographic phase change (Augustyn et al. 2014). Underpotential deposition and redox pseudocapacitance represent charge storage on the surface; however, in intercalation pseudocapacitance, charge storage does not occur on the surface but in the bulk material (Augustyn et al. 2013). Figure 6.5 shows the schematics of the double capacitors, the pseudocapacitance and the working potential windows of many oxide materials in aqueous electrolyte with the average working potential of above 0 V vs. SCE.

6.1.2 *Design and Synthesis of the Transition Metal-Oxides-Based Materials for Application in Supercapacitors (SCs)*

In order to keep the effectiveness of the electrochemical energy storage technology to improve the advancement of renewable energy sources, several important requirements should be considered during the design and selection of the suitable electrode material. These desired requirements include (1) high stability in various types of electrolyte solution, (2) high resistance against electrochemical corrosion and (3) good electronic conductivity. Nanomaterials of about the length scale of less than 100 nm have received increasing interest, owing to their fundamental scientific significance as well as their potential applications that is derived from their fascinating electrical, magnetic and catalytic properties (Burda et al. 2005; Tan et al. 2011). As compared to the bulk active electrode materials, the corresponding nanomaterials possess outstanding electrochemical activity, such as higher capacitance, larger surface areas and relatively good conductivity; thereby, nanomaterials have vast potential application in the electrochemistry field. Many transition metal oxides (TMOs) and metal hydroxide (Johan E. ten Elshof et al. 2016) give rise to faradaic reaction that offers high specific capacity and high energy densities due to their rich electrochemistry and have been extensively explored as supercapacitive materials due to their high power and energy output through nanostructuring and materials engineering. Consequently, metal oxides (MOs) with various chemistries (i.e. simple, double or mixed metal oxides, nanostructures, composites, etc.) have been investigated as high-performance electrode materials for pseudocapacitive application. The studied MOs in this chapter include RuO_2 (Xia et al. 2012), MnO_2 (Bello et al. 2013b; Makgopa et al. 2015), SnO_2 (Yan et al. 2010), V_2O_5 (Wei et al. 2012), Fe_2O_3 (Zhou et al. 2012), Fe_3O_4 (Wu et al. 2003), Bi_2O_3 (Gujar et al. 2006), WO_3 (Deb 2008; Zheng et al. 2011) and In_2O_3 (Chang et al. 2008). Conducting polymers (CPs) have also attracted attention and are among the most promising pseudocapacitor materials for flexible supercapacitors, motivating the existing energy storage devices towards the future advanced flexible electronic applications due to their high redox active-specific capacitance and inherent elastic polymeric nature (Shown et al. 2015). Similarly, metal nitrides/oxynitrides have shown emerging properties compared to the metal oxide and in some cases show better and interesting result and therefore have attracted attention as an emerging supercapacitor electrode beyond oxide (Ghosh et al. 2018).

6.1.2.1 Ruthenium Oxide (RuO_x)

At the early stages of exploring MOs as suitable electrode material for supercapacitor applications, RuO_2 emerged as a promising and predominant candidate in energy storage due to its excellent electrical characteristics, thermal stability and other unique electrochemical properties such as high specific capacitance.

Therefore, the above-mentioned properties made RuO_2 to be one of the most extensively studied electrode materials for supercapacitor applications. Ruthenium is a multivalence rare metal element, hard, brittle and light grey in colour (Zheng et al. 1995; Li et al. 2018). As a group of multifunctional material, Ru-based materials family include ruthenium dioxide (RuO_2), hydrous ruthenium dioxide ($RuO_2{\cdot}xH_2O$), ruthenium oxide (RuO_x), ruthenium (Ru) and their composites (Vijayabala et al. 2018). There are two phases of RuO_2: a crystal phase (RuO_2, rutile phase) and an amorphous hydrous phase ($RuO_2{\cdot}xH_2O$). The efficiency of Ru-based materials depends on variety of factors, but their overall performance strongly rests with the surface area that can result from the careful selection of the method of preparing the desired material (Wang et al. 2016a; Li and He 2018). The synthesis of Ru-based nanomaterials has been achieved via various synthetic routes such as wet chemical, vapour phase, hydrothermal and biological and also through various synthetic methods such as thermal decomposition, sol–gel process, electrostatic spray deposition and electrodeposition, among others (Hu et al. 2006; Yin et al. 2012; Park et al. 2015; Li et al. 2018; Vijayabala et al. 2018). From the above synthetic methods, the hydrothermal technique displayed several advantages, such as one-step synthesis method, low aggregation level and narrow crystallite size distribution, over the other synthetic methods (Yin et al. 2012). In addition, the high purity and excellent control over the morphology and size of the particle have been achieved by control of the nucleation and growth owing to its surfactant or protective agent (Park et al. 2015; Vijayabala et al. 2018). During this process, surfactants such as cetyltrimethylammonium bromide (CTAB), hexamethylenetetramine (HMT), polyethylene glycol (PEG), citric acid, citrate potassium, ethylenediamine (EDA) or polyethylene glycol (PEG) are used to control the morphology of the materials (Vijayabala et al. 2018). Several architectures of different morphologies of Ru-based material ranging from one-dimensional (1D) nanostructures, nanorods and nanosheets were synthesized in the presence and absence of the surfactant. The quest for other suitable and cheaper electrode materials with excellent electrochemical properties similar to RuO_2 has been explored. In addition, these RuO_2 capacitor-type materials are only suitable for aqueous electrolytes, thus limiting the nominal cell voltage to 1.0 V. In order to manipulate the morphology of RuO_2, the annealing temperature is a key factor affecting the morphology, which exists usually in the form of nanostructure such as nanoparticle, nanorod and nanofiber. High annealing temperature, for example, from 300 to 800 °C, leads to the crystalline phase of RuO_2 and less water content, resulting in the change of the number of active reaction sites, as well as the electron and proton conductivity (Park et al. 2015). Synthesis of the RuO_2 nanocatalyst is shown in Fig. 6.6. A schematic diagram for the fabrication of RuO_2 nanowires and 3D RuO_2 branched Au-TiO_2 nanostructure can be clearly observed in Fig. 6.6a, and the above results were supported by the top-view SEM images of RuO_2 nanowires and 3D branched nanostructures (Fig. 6.6b, c). A simple and cheap way of synthesising RuO_2 nanocatalyst with various morphologies can be obtained by following the route in Fig. 6.6d, e).

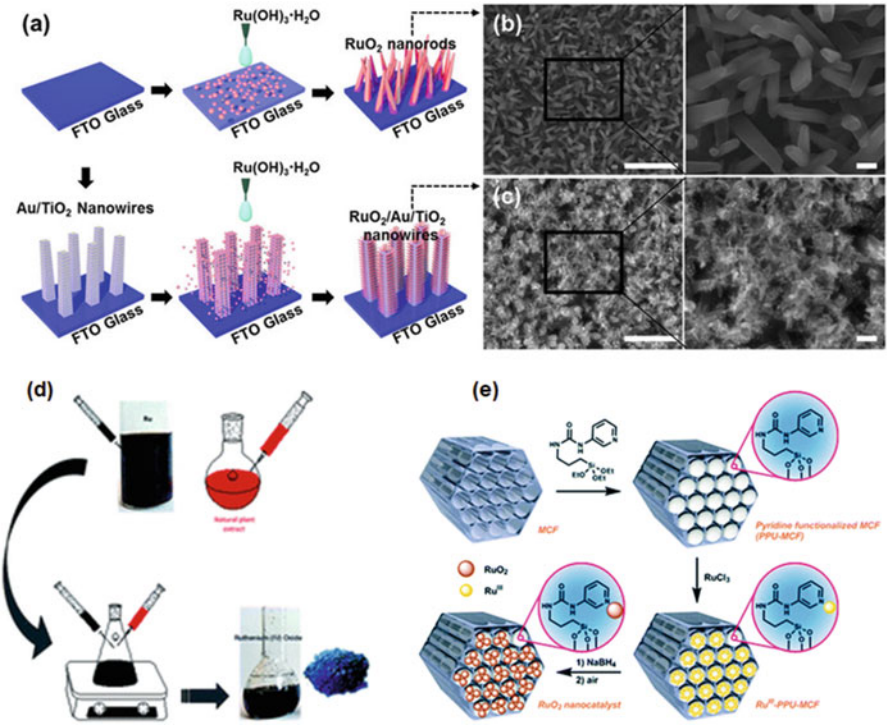

Fig. 6.6 (**a**) Schematic diagram for the fabrication of RuO_2 nanowires and 3D RuO_2 branched Au-TiO_2 nanostructure, (**b, c**) top-view SEM images of RuO_2 nanowires and 3D branched nanostructures (scale bars in the left and right images, 1 μm and 100 nm, respectively) (With permission of Park et al. 2015) and (**d, e**) synthesis of the RuO_2 nanocatalyst ((**d**), with permission of Li et al. 2018, and (**e**), with permission of Gustafson et al. 2017)

It is well known that RuO_2 is a good cathode material for electrochemical capacitors due to the fact that its hydrous form can reversibly store 150–260 F cm^{-2} in aqueous electrolytes or approximately ten times the double-layer capacity of carbon (Zheng et al. 1995). This material stores charge by reversibly accepting and donating protons from an aqueous electrolyte governed by the potential dependent equilibrium of Eq. 6.7.

$$RuO_2 + \delta H^+ + \delta e^- \leftrightarrow RuO_{2-\delta}(OH)_\delta; 0 \leq \delta \leq 2 \tag{6.7}$$

Due to the lack of abundance and the expensive cost of the noble metallic element ruthenium (Ru), there are drawbacks for its commercial application in supercapacitors (SCs), leading to the reduced use of this electrode for SC applications. However, in order to improve the electrochemical properties of other materials that have limited application in energy storage, Ru-based nanomaterials are being explored resulting in Ru-based composites. Miller and co-workers (Miller 1997)

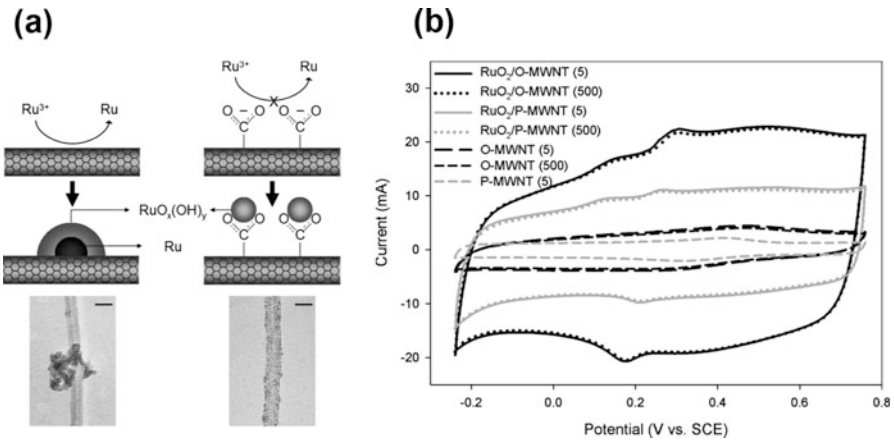

Fig. 6.7 (**a**) Schematic diagram of the different formation mechanisms of RuO_2 on P-MWNT and O-MWNT in the preparation process and their actual TEM images (scale bar = 20 nm) and (**b**) cyclic voltammograms in 1 M H_2SO_4 electrolyte with a scan rate of 20 mV s^{-1} (With permission of Kim and Mitani 2006)

have demonstrated the specific capacitance of ruthenium nanoparticles deposited on the surface of the carbon aerogels to be 330 F g^{-1}, while Zheng and co-workers (Zheng et al. 1995) have reported values as high as 768 F g^{-1} in the early and mid-1990s. Other researchers explored various synthetic routes of making Ru-based nanocomposites by using functionalized carbon nanotubes as supports to these nanoparticles. The surface carboxyl groups from the acid-functionalized carbon nanotubes (CNTs) are able to protect against spontaneous reduction into disadvantageous Ru metal through blocking the contact between MWCNT surfaces and Ru ions by certain bond formation. The as-mentioned mechanism above is presented in schematic form in Fig. 6.7a. The electrochemical performance of the synthesized Ru-Carbon nanocomposite shown in Fig. 6.7b exhibits quite large difference in capacitance behaviour between RuO_2/P-MWNT and RuO_2/O-MWNT, with capacitance values of 182 and 304 F g^{-1}, respectively. The results obtained in this study are lower than other Ru-based results obtained from the literature. However, the ability to reduce the usage of Ru alone but substitute it with other cheap materials and yet obtain such promising capacitive performance emphasizes the promise that lies ahead in terms of developing cheap yet effective Ru-C composite SC devices.

Hwang and co-workers (2015) demonstrated a simple one-step process for the synthesis and processing of laser-scribed graphene (LSG) and RuO_2 nanocomposites fabricated into electrodes that exhibit ultrahigh energy and power densities. The high voltage asymmetric electrochemical capacitors made-up of LSG/RuO_2 as positive electrode and AC as negative electrode showed improved electrochemical performance as shown in Fig. 6.8. The asymmetric electrochemical capacitor demonstrated extremely high energy density of 55 Wh kg^{-1} at a power density of 12 kW kg^{-1}, placing it among the best-performing hybrid electrochemical capacitors.

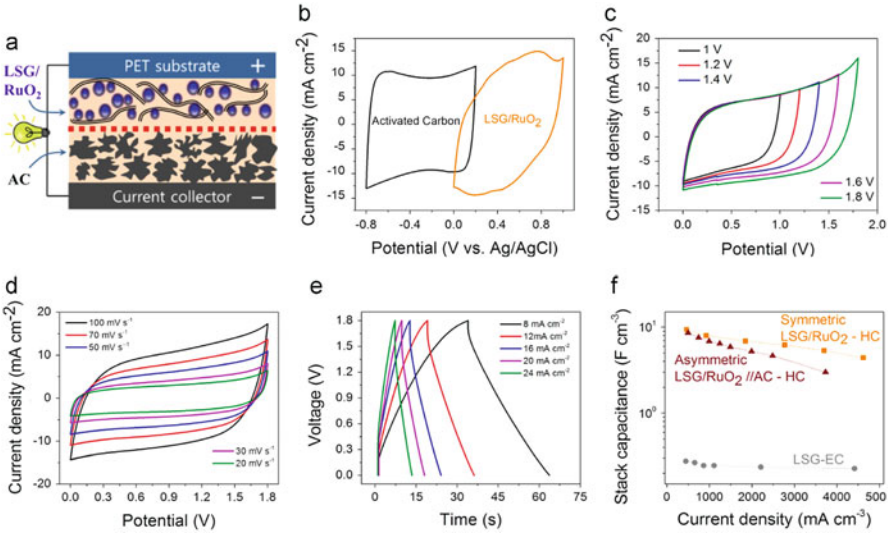

Fig. 6.8 Electrochemical performance of an asymmetric LSG/RuO_2//AC SCs. (**a**) Illustration of the structure of asymmetric SCs assembled with LSG/RuO_2 +ve electrode and activated carbon −ve electrode. (**b**) CV curves comparing the electrochemical properties of the +ve and −ve electrodes in their stable operating voltage windows, obtained at 70 mV s^{-1}. (**c**) CV curves of the asymmetric SCs at increasing voltage window from 1.0 to 2.0 V, all acquired at 70 mV s^{-1}. (**d**) CV performance of the asymmetric supercapacitor at different scan rates tested at a maximum voltage of 1.8 V. (**e**) Galvanostatic charge and discharge curves of the asymmetric supercapacitor collected at different current densities. (**f**) Evolution of the capacitance of the cell stack (including the current collector, active material, electrolyte and separator) as a function of the applied specific current for symmetric LSG/RuO_2, asymmetric LSG/RuO_2//AC and LSG SCs (With permission of Hwang et al. 2015)

Recently, Jiang and co-worker (2018) have managed to integrate the Ru nanoparticles on the 2D transition metal carbides and nitrides, known as MXenes instead of the carbon nanomaterials employed in the literature and tested them for SC applications (Fig. 6.9). They have demonstrated that the hydrophilicity of MXenes combined with their metallic conductivity and surface redox reactions which is the key for high-rate pseudocapacitive energy storage in MXene electrodes can be used to support electrode materials that have good theoretical capacitive performance but yet limited in applications due to the poor conductivity. Their study utilized titanium carbide MXene ($Ti_3C_2T_x$) as negative electrode in acidic electrolyte while ruthenium oxide (RuO_2) as positive electrode. The asymmetric device operated at a voltage window of 1.5 V and managed to deliver an energy density of 37 μW h cm^{-2} at a power density of 40 mW cm^{-2}, with 86% capacitance retention after 20,000 charge–discharge cycles.

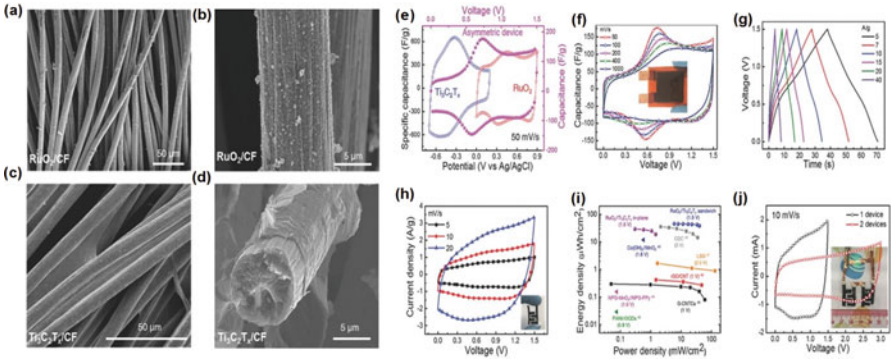

Fig. 6.9 (**a**) Low- **and** (**b**) high-magnification FESEM images of RuO_2/CF. (**c**) Low-magnification SEM image showing uniform coating of $Ti_3C_2T_x$ on carbon fibres. (**d**) Wrapped $Ti_3C_2T_x$ flakes over an individual fibre of the carbon fabric. (**e**) CVs of RuO_2/CF, $Ti_3C_2T_x$/CF and the asymmetric device at a scan rate of 50 mV s^{-1}. (**f**) CVs of RuO_2//$Ti_3C_2T_x$ asymmetric sandwich device at different scan rates, inset shows the digital photograph of the asymmetric device. (**g**) Galvanostatic charge–discharge curves at different current densities. (**h**) CVs of asymmetric in-plane device; inset shows optical image for the in-plane solid-state device attached to polypropylene substrate. (**i**) Ragone plot displays real energy and power densities of RuO_2//$Ti_3C_2T_x$ device in comparison with the other state-of-the-art microsupercapacitors, square represents carbon-based microsupercapacitors, triangle represents pseudocapacitive asymmetric microsupercapacitors. (**j**) Cyclic voltammograms of the RuO_2//$Ti_3C_2T_x$ tandem in-plane devices at scan rate of 10 mV s^{-1} (inset shows that two devices connected in series can power up a green LED during the discharge state) (With permission of Jiang et al. 2018)

6.1.2.2 Manganese Oxide (Mn_xO_y)

Manganese oxide (Mn_xO_y)-based electrode materials (i.e. MnO_2, Mn_3O_4, Mn_2O_3 and MnO) and its derivatives have been studied as the alternative electrode material in supercapacitors due to their contrasting properties as compared to RuO_2. The Mn_xO_y-based electrode materials and their derivatives have demonstrated to be environmentally friendly while being relatively cheap and abundant in nature. Apart from the socio-economic benefits of the Mn_xO_y-based materials and their derivatives, these electrode materials are also characterized by their relatively high theoretical specific surface area (i.e. MnO_2, 1370 m^2 g^{-1}), multiple crystal phases, high theoretical capacitance and good electrochemical response (Subramanian et al. 2005; Yan et al. 2009; Wu et al. 2010; Wang et al. 2012c; Yu et al. 2013b; Jafta et al. 2013; Chidembo et al. 2014; Borgohain et al. 2014). Manganese oxide displays various oxidation states and phases, and the most often studied phases of Mn_xO_y-based materials are MnO_2 having an oxidation state of +4, Mn_2O_3 having an oxidation state of +3 and Mn_3O_4 having an oxidation state of both +2 and +3. The MnO_2 nanomaterials further exhibit various crystallographic forms depending on the types of structural phases (i.e. -, -, γ-, -, ε- and -types) that are dominant during synthesis, as shown in Fig. 6.10 (Xiao et al. 2009). They can also be identified in their various mineral forms such as birnessite, hausmannite, pyrolusite, manganite,

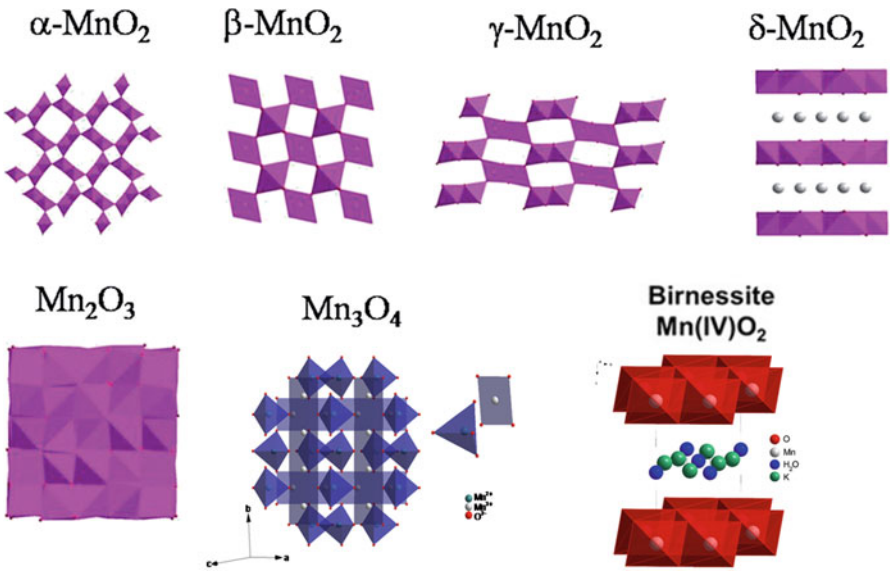

Fig. 6.10 Different Mn_xO_y crystal structures With permission of Liu et al. 2015c)

manganosite and psilomelane (Potter and Rossman 1979; Fan and Yang 1999; Wei et al. 2011). Several structural forms of MnO_2 with different nanoarchitectures such as nanowires (Wang et al. 2014; Yin et al. 2014), nanorods (Wu et al. 2013), single crystal nanotubes (Xiao et al. 2009), nanourchins (Xu et al. 2007) and amorphous (Hatzell et al. 2014) have been synthesized using hydrothermal techniques. Some other techniques used for the synthesis of MnO_2 nanostructures include thermal decomposition, co-precipitation (Lee and Goodenough 1999; Brousse et al. 2006; Nam et al. 2010), simple reduction (Ni et al. 2009; Ragupathy et al. 2009), sol–gel (Wang et al. 2005, 2007), solid-state process and microwave process (Meher and Rao 2012; Ming et al. 2012; Bello et al. 2013a). The other rising Mn_xO_y material in the literature is manganese (II, III) oxide with the chemical formula Mn_3O_4. It is found in nature as the mineral hausmannite and is made of a spinel structure with tetragonal distortion elongated along the c-axis due to Jahn-Teller effect on the Mn^{3+} ion. Manganese ions occupy the octahedral B-site (Mn^{3+}) and tetrahedral A-site (Mn^{2+}) corresponding to a normal spinel structure (Fig. 6.10). Several studies have been conducted in order to improve Mn_3O_4 electrode materials in SC application. Subsequently, to improve the electrochemical capacitive behaviour of Mn_3O_4, the nanosized particles of Mn_3O_4 have been prepared by various methods such as successive ionic layer adsorption and reaction (SILAR) (Dubal and Holze 2013), hydrothermal (Yang et al. 2015), solution combustion (Gao et al. 2011), chemical bath deposition (Xu et al. 2006), sonochemical (Baykal et al. 2010) and microwave techniques (Zhou et al. 2011; Sankar et al. 2012). Different nanoarchitectures of Mn_3O_4 particles such as single crystals, nanocrystals, nanocubics, nanorods, microspheres and interlocked cubes have been successfully synthesized and tested for SC

application (Dubal et al. 2009, 2010; Sankar et al. 2012; Wang et al. 2012; Lee et al. 2012; Dong et al. 2013). Manganese (III) oxide, Mn_2O_3, and manganese (II) oxide, MnO, are other types of the oxides of the Mn_xO_y-based derivatives. The Mn_2O_3 type exists in two recognizable forms, α-Mn_2O_3 and γ-Mn_2O_3. The α-Mn_2O_3 has the cubic bixbyite structure, while pure Mn_2O_3 has an orthorhombic structure, and γ-Mn_2O_3 has a structure related to the spinel structure of Mn_3O_4 with the oxide ions closely packed in cubic form (Wells 1984). A MnO, just like any monoxides, adopts the rock salt structure, with anions and cations being both octahedrally coordinated (Greenwood 1997). Just as much as any manganese oxide material, Mn_2O_3 nanospheres have been synthesized using hydrothermal and sonochemical techniques by Nathan et al. as an EC electrode material (Nathan et al. 2008). Chen et al. has successfully synthesized γ-Mn_2O_3 nanowire bundles (Chen et al. 2005). Recently, Li et al. synthesized nanocubic Mn_2O_3 using hydrothermal technique for the EC application (Li et al. 2015). Nano-sized manganese oxide (Mn_2O_3) was synthesized by Chiang et al. using a solvothermal technique (Chiang et al. 2006). There is a limited literature on the synthesis of Mn_2O_3 for EC application even though several of these materials have been widely synthesized using various techniques such as chemical oxidation (Chen et al. 1997), calcination of MnO_2 and hydrothermal (He et al. 2003).

Several studies on electrochemical behaviour of MnO_2-based materials and its derivatives in an aqueous electrolyte have been conducted in order to better understand their mechanism of charge storage on the surface of the electrode. Hydrated manganese oxides exhibit specific capacitances within the range of 100–200 F g^{-1} in alkaline electrolyte. The surface reaction occurring at the MnO_2 electrode involves the adsorption of electrolyte cations (C+ = H+, Li+, Na+ and K+) on the MnO_2-based materials, whereas the bulk faradaic reaction relies on the intercalation or de-intercalation of electrolyte cations in the bulk of the manganese oxide and is illustrated by Eqs. 6.7 and 6.8, respectively, (Toupin et al. 2004; Yang et al. 2014):

$$(MnO_2)_{surface} + C + + e^- \leftrightarrow (MnO_2{}^- C^+)_{surface} \tag{6.8}$$

$$MnO_2 + C^+ + e^- \leftrightarrow MnOOC \tag{6.9}$$

In the established charge storage mechanisms, a redox reaction between the III and IV oxidation states of Mn ions occurs (Yang et al. 2014). Dedicated approach on the synthesis of MnO_2-based materials and the electrolyte type played a major role on the electrochemical outcome of its SC applications. An amorphous hydrous manganese oxide (α-$MnO_2{\cdot}nH_2O$) was anodically deposited onto a graphite substrate showing an improved maximum specific capacitance of 330 F g^{-1} and 320 F g^{-1} achieved from cyclic voltammetry and galvanostatic charge-discharge measurements, respectively, using Na_2SO_4 (0.1 M) as electrolyte (Hu and Tsou 2002). However, due to the high resistivity of α-$MnO_2{\cdot}nH_2O$, a conducting additive, such as carbon materials, CNTs or graphene and OLCs, is required for the realization of EC electrodes (Cottineau et al. 2006; Sharma et al. 2007). As a result, α-MnO_2 has been decorated on the SWCNT by a simple precipitation technique with good cycle

power at the specific current of 2 A g^{-1} (Subramanian et al. 2006). Ma et al. (2008) synthesized a birnessite-type MnO_2 coated uniformly on multi-walled carbon nanotubes (CNTs) with specific surface area of 200 m^2 g^{-1} by using a spontaneous direct redox reaction between the multi-walled CNTs and permanganate ions (MnO_4^-) with a high specific capacitance of the MnO_2/CNT nanocomposite in an organic electrolyte of ca. 250 F g^{-1} at a high specific current of 1 A g^{-1}. Jafta et al. (2013) synthesized α-MnO_2 from the raw electrolytic manganese dioxide (EMD) using hydrothermal technique in the presence of a sodium dodecyl sulphate (SDS) surfactant and decorated them on the surface of the graphene oxide (GO). The electrochemical properties of nanostructured α-MnO_2/GO composite fabricated in an aqueous asymmetric electrochemical capacitor exhibited high energy density of 35 Whkg^{-1} and specific capacitance of 280 F g^{-1} at high voltage window of 1.8 V using 1 M Li_2SO_4 as electrolyte. The electrochemical behaviour of vertical graphene nanosheets (VGNs) and MnO_2 was also investigated; the VGNs provide controlled porous structure and high electrolyte accessible surface area for multiple pathways for ion transport. The charge storage behaviour of the MnO_2/VGNs was excellent exhibiting a high areal capacitance of 5.6 mF/cm^2, which is 110 times higher than that of VGNs (51.95 μF/cm^2) at 50 mV s^{-1}. The enhanced capacitance is attributed to the highly conductive 3D network of VGNs which provide fast electron and ion transport and also a large pseudocapacitance from MnO2 coating (Ghosh et al. 2016). Makgopa et al. (2015) showed that the use of birnessite-type MnO_2 decorated on highly graphitized onion-like carbon (OLC) can improve the electrochemical performance of the MnO_2. The nanocomposite of OLC/MnO_2 shown by the FESEM images (Fig. 6.11a, b) displayed better interaction and was fabricated on a symmetrical two-electrode device using the Ni foam as a current collector (Fig. 6.11c, d,) and exhibited a large specific capacitance of 254 F g^{-1} and a remarkably high power density of 74.8 kW kg^{-1}. The surface morphologies of OLC/MnO_2 nanohybrid are shown in Fig. 6.11a (FESEM) and in Fig. 6.11b (TEM) which indicates clear interactions of the precursor material with each other for good capacitive performance. The SAED pattern in the inset (Fig. 6.11b) shows lattice fringes for crystalline MnO_2 and circular lattice shells for OLC confirming the synergistic effect from the nanocomposites.

Manganese (II, III) oxide (Mn_3O_4) as a potential electrode material for ECs showed up just after the researchers discovered MnO_2 as pseudocapacitive electrode material. In 2003, a thin film Mn_3O_4 electrode material was reported to have displayed specific capacitance of 92 F g^{-1} in aqueous electrolyte and 58 F g^{-1} in organic electrolyte from cyclic voltammetry at the scan rate of 20 mV s^{-1} (Jiang and Kucernak 2002). Wu and Hu (2005) studied a mixture, consisting of Mn_3O_4 and MnOOH crystals and reported specific capacitance ranging between 45 and 71 F g^{-1}, and Djurfors et al. (Djurfors et al. 2005) showed that Mn_3O_4 film prepared by either thermal or electrochemical oxidation of Mn/MnO films has an effect on the capacitive performance of the electrode material. Nagarajan et al. (2006) later followed the principle of Djurfors et al. to form a spinel Mn_3O_4 phase at 300 °C with an improved specific capacitance value of 445 F g^{-1} in Na_2SO_4 electrolyte. As a race in finding a stable and suitable electrode derived from the Mn_3O_4 material,

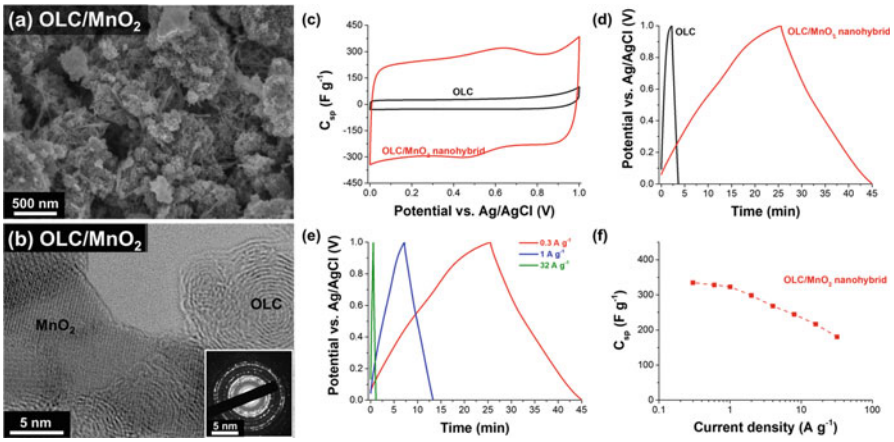

Fig. 6.11 (**a**) SEM (**b**) TEM images of the OLC/MnO_2 nanohybrid (the inset is the corresponding SAED pattern of (**b**)), (**c**) cyclic voltammograms at 5 mV s^{-1} and (**d**) galvanostatic charge–discharge curves at 0.3 A g^{-1} comparing OLC and the OLC/MnO_2 nanohybrid, (**e**) galvanostatic charge–discharge curves for the OLC/MnO_2 nanohybrid at various current densities and (**f**) C_{sp} vs. current densities of the OLC/MnO_2 nanohybrid. Three-electrode configuration with nickel foam as the current collector. Electrolyte: aqueous 1 M Na_2SO_4 (With permission of Makgopa et al. 2015)

researchers developed composites of this material from carbon templates. In 2008, Mn_3O_4/MWCNT composite was examined using cyclic voltammetry and obtained a maximum specific capacitance of 330 F g^{-1} (An et al. 2008). Wang et al. (2010) later used graphene sheet as a template for decoration of Mn_3O_4 by mixing graphene suspension in ethylene glycol with MnO_2 organosol, followed by subsequent ultrasonication processing and heat treatment. The as-prepared Mn_3O_4/graphene nanocomposite gave a specific capacitance of 175 F g^{-1} in Na_2SO_4 electrolyte and 256 F g^{-1} in KOH electrolyte. The higher result obtained in the alkaline medium is due to the higher ionic conductivity of the electrolyte compared with the neutral electrolyte. As it has been shown from the literature, the hydrated ion size (3.31 Å for K^+ and 3.58 Å for Na^+) and ionic conductivity (73.5 S cm^2 mol^{-1} for K^+ compared to 50.11 S cm^2 mol^{-1} for Na^+) play a crucial role in electrochemical performance of carbon electrode materials (Zhong et al. 2015). Similarly, the ionic radius of the hydrated negatively charged anions contributes to the EDL behaviour via electroadsorption, and the sizes are in the following order OH^- (3.00 Å) < NO_3^- (3.35 Å) < SO_4^{2-} (5.33 Å) (Zhong et al. 2015). Hence, the alkaline electrolyte is expected to give the best electrochemical performance taking into account electrode that could easily accommodate the smaller size of K^+ and the electroadsorption of the negatively charge anions (OH^-), coupled with it better conductivity and ionic mobility. Qiao et al. (2015) synthesized micro/nanostructured Mn_3O_4 with an open 3D flower-like morphology by a facile solvothermal approach using hexadecyltrimethylammonium bromide as a surfactant and ethanol as a solvent. The Mn_3O_4 microspheres used exhibited electrochemical performance with a

specific capacitance of 286 F g^{-1} at a low specific current (0.5 A g^{-1}) and still retained 80% (230 F g^{-1}) and 73% (210 F g^{-1}) at higher current densities of 5 A g^{-1} and 10 A g^{-1}, respectively. The enhanced capacitive performance of Mn_3O_4/graphene nanocomposites was attributed to the nanoparticulate nature of Mn_3O_4 nanoparticles and functional groups attached to graphene nanosheets. Recently, Makgopa et al. (2017) reported on the electrochemical performance of the tetragonal hausmannite Mn_3O_4, when embedded on various carbon materials to form OLC/Mn_3O_4, CNT/Mn_3O_4, GO/Mn_3O_4 and AC/Mn_3O_4 nanohybrids, and investigated as electrode material for symmetric, as shown in Fig. 6.12, and asymmetric pseudocapacitor device. The nanohybrid electrode materials demonstrated higher electrochemical performance (in terms of specific capacitance and rate capability as energy storage devices) compared to the pure Mn_3O_4. The OLC/Mn_3O_4 nanohybrid was shown to be the best-performing symmetric pseudocapacitor device, and it exhibited higher specific capacitance of 195 F g^{-1}, specific energy of 4.3 Wh kg^{-1} and power density of 52 kW kg^{-1} compared to other carbon nanohybrid materials studied. When it was tested as a high-voltage asymmetric pseudocapacitor device, the OLC/Mn_3O_4 nanohybrid displayed maximum energy and power densities of ca. 19 Wh kg^{-1} (at 0.1 A g^{-1}) and 45 kW kg^{-1} (at 10 A g^{-1}), respectively. The high performance of the OLC-based system compared to the other carbon systems is ascribed to the combined unique intrinsic properties of the OLC, high electrical conductivity, highly accessible outer surface and large interparticle pore volumes. The above properties have ensured OLC/Mn_3O_4 nanohybrid as a suitable candidate for the high-voltage asymmetric pseudocapacitor device.

To the best of our knowledge, there is no much literature on the use of Mn_2O_3 and MnO as SC applications. The study of Mn_2O_3 as electrode material for supercapacitors surfaced at around 2006, when Chiang et al. (2006) reported on the synthesis and the examination of the nanoparticles of Mn_2O_3 as a potential SC electrode material. The electrode material exhibited a maximum specific capacitance of about 197 F g^{-1} from cyclic voltammetry at the scan rate of 10 mV s^{-1}. Yu et al. (2008) reported on the synthesis of Mn_2O_3 particles that were made of micropores having a specific capacitance of 350 F g^{-1}. The improved performance was attributed to the relatively high specific surface area of 283 m^2 g^{-1}. Zhang et al. (2009) reported on the nano-sized Mn_2O_3 which was homogenously incorporated on a mesoporous carbon template exhibiting an improved specific capacitance of 600 F g^{-1}. In 2011, Wang et al. (2011) reported a composite of Mn_2O_3 and carbon aerogel microbead (CAMB), a maximum specific capacitance of 368 F g^{-1}, and it was emphasized the fact that this type of manganese oxide material is well suited for EC applications. Li et al. (2015) developed porous Mn_2O_3 nanocubins through hydrothermal technique that was followed by calcination in the air which exhibited a specific capacitance of 191 F g^{-1} at a specific current of 0.1 A g^{-1}. This electrode material showed relatively high rate capability at high specific current of 5.0 A g^{-1} and excellent long-term cycle stability even after 3000 cycles. The enhanced rate capability of this material was associated with the improved porosity. Mn_2O_3-based electrode materials are potentially useful as supercapacitor electrode materials, albeit its growth or attention has been dramatically slow compared to other manganese

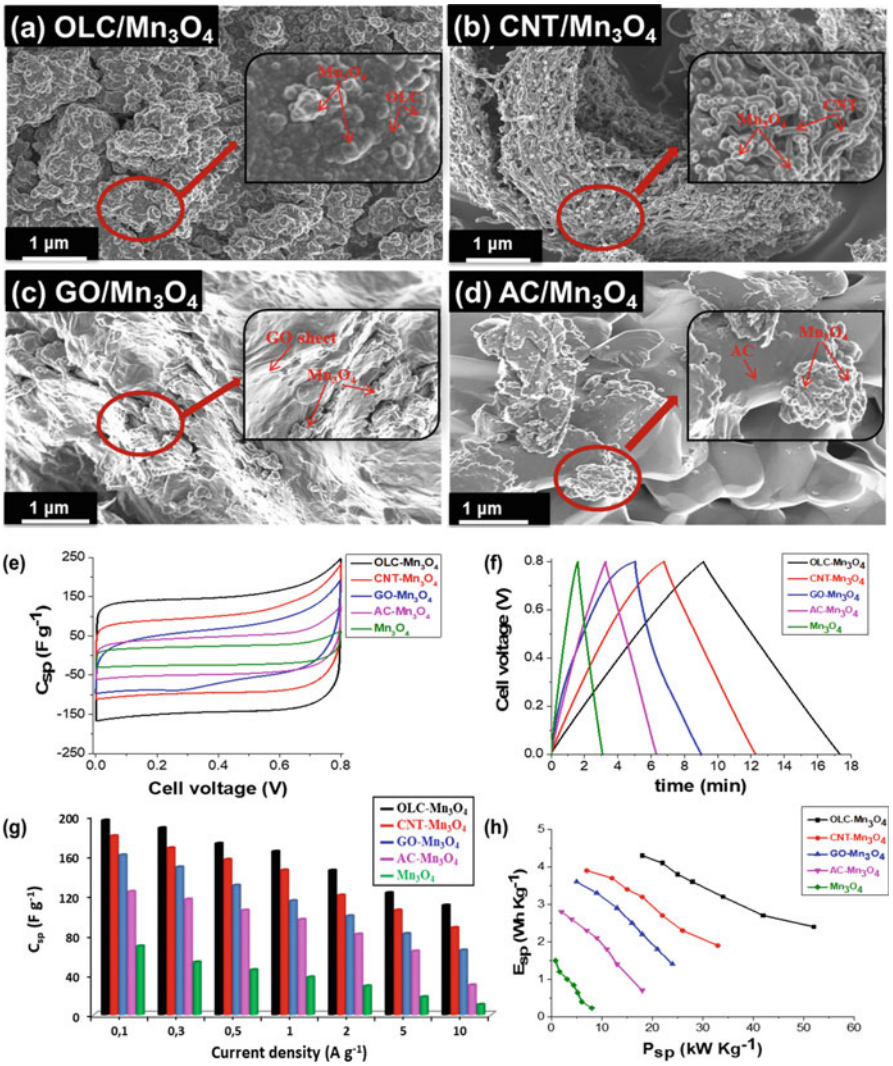

Fig. 6.12 SEM images of (**a**) OLC/Mn_3O_4, (**b**) CNT/Mn_3O_4, (**c**) GO/Mn_3O_4 and (**d**) AC/Mn_3O_4 nanohybrids. Inset in (**a**–**d**) is the high-magnification SEM image of respective nanohybrids. Comparative (**e**) cyclic voltammograms at 5 mV s^{-1}, (f) galvanostatic charge-discharge curves at 0.3 A g^{-1}, (**g**) Csp vs. specific current plot and (**h**) energy vs. power densities, for OLC/Mn_3O_4, CNT/Mn_3O_4, GO/Mn_3O_4, AC/Mn_3O_4 nanohybrids and Mn_3O_4 in aqueous 1 M Na_2SO_4 (With permission of Makgopa et al. 2017)

oxide-based electrode such as MnO_2 and Mn_3O_4. To the best of our knowledge, there is no literature on the use of manganese mono-oxide (MnO) as an electrode material for SC application. For more information on this Mn_xO_y-based electrode material, the reader is referred to the book chapter by Makgopa et al. (2016).

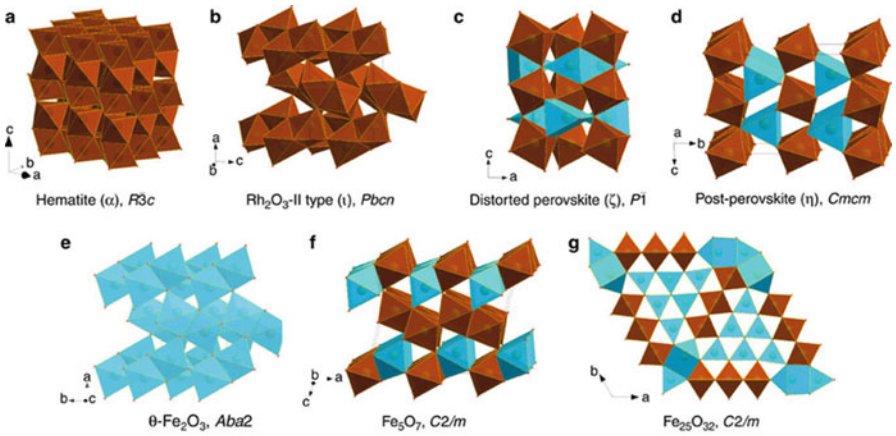

Fig. 6.13 Crystal structures of iron oxide phases. Building blocks are octahedral (brown) and trigonal prisms (blue) (With permission of Bykova et al. 2016)

6.1.2.3 Iron Oxide (Fe_xO_y)

Iron oxide (Fe_3O_4) is another cheap alternative to RuO_x and has attracted attention in several fields of application due to its favourable magnetic, electric and optical properties (Ozkaya et al. 2009) and has been chosen as a potential electrode material in energy storage due to its high theoretical capacity (924 mA h g^{-1}), natural abundance, low cost, good chemical stability, environmental friendliness and cost-effectiveness (Wang et al. 2008). Similar to the manganese discussed above, different crystal structures can easily lead to pathway for the synthesis of these materials. Figure 6.13 shows the various enigmatic structural, electronic and magnetic transformations at high pressures and high temperatures.

They have been predominantly investigated as anode in Li-ion batteries, showing high- performance capability when the morphologically or compositionally is properly engineered (Luo et al. 2013). For SC applications, they are suitable as negative electrodes for hybrid devices due to their broad potential window of operation (1–1.2 V) in aqueous solutions (Qu et al. 2011). The preliminary evaluations revealed that the relatively low electrical conductivity of these oxides requires the introduction of conductive additive such as CB to increase its conductivity and boost its capacitance. In addition, it has been already demonstrated in several studies that combining these oxide materials with carbonaceous materials leads to high values of conductivity and can improve the overall electrochemical behaviour due to synergistic effects between the oxide and the carbon material. The capacitive nature of Fe_3O_4 has been investigated by Wu et al. (2003) in various electrolytes, and it was shown with a high capacitance value of 510 F g^{-1}. Similarly, it has been shown that Fe_2O_3 can operate in a wide negative potential window of 0 to −1.35 V; such an excellent supercapacitive performance makes it a perfect anode electrode material (Tang et al. 2015). The reaction governing the performance of aqueous electrolytes

such as Na_2SO_3, Na_2SO_4 and KOH (Wang et al. 2006) was established using an electrochemical quartz crystal microbalance and X-ray photoelectron spectroscopy. It was found that the capacitance of Fe_3O_4 in the Na_2SO_3 electrolyte arises due to the combination of both the EDLC and pseudocapacitor involving the reduction/oxidation of specifically adsorbed sulphite anions given by the equations below. In the Na_2SO_4 solution, the performance was due to the formation of a double layer, and in the KOH, the performance arises due to partial surface oxidization of the oxide electrode.

$$2SO_3^2 + 3H_2O + 4e \leftrightarrow S_2O_3^2 + 6OH \tag{6.10}$$

$$2SO_3^2 + 3H_2O + 8e \leftrightarrow 2S^2 + 6OH \tag{6.11}$$

Quite a number of Fe_3O_4 electrodes have been reported, for example, Fe_3O_4 films made by electroplating technique exhibited a specific capacitance of 170 F g^{-1} in Na_2SO_3 (Wang et al. 2006), and Fe_3O_4 nanoparticles with a specific capacitance of 185 F g^{-1} was reported via a sol–gel technique (Mitchell et al. 2014). However, the capacitance reported is far below the theoretical value, which is because of low electronic conductivity, and morphology collapse, which often leads to low electrochemical performance and poor cycling performance. To build on the exhibiting and maximize the performance of SCs, it is necessary to develop hybrid electrode materials, combining electric double-layer capacitive materials and pseudocapacitive materials such as Fe_3O_4. Thus, Fe_3O_4 has been included in many carbon matrices to improve the overall capacitance of the system because of the good electrical conductivity and excellent electrochemical stability (Sevilla and Mokaya 2014; Meng et al. 2014). These Fe_3O_4–carbon composites showed improved electrochemical performance compared to the individual components due to a positive synergy between Fe_3O_4 and carbon materials, and their charge storage arises from both the double-layer and faradaic reactions. For example, cubic Fe_3O_4 and graphene layer assembled into a symmetric supercapacitor device with the specific capacitance ~782 F g^{-1} at a specific current of 3 A g^{-1} (Xu et al. 2008). An Fe_2O_3 decorated with single-walled carbon nanotubes (SWCNT) as flexible anodes in LIBs with a discharge capacity of 801 mA h g^{-1} after 90 cycles was reported by Zhou et al. (2012). The excellent result obtained was attributed to the conductivity of the SWCNT. Min et al. (2017) reported a facile and efficient technique to synthesize porous iron oxide coated with graphene as was tested as electrode materials for lithium–ion batteries and supercapacitors. The encapsulation of porous Fe_2O_3 and Fe_3O_4 nanorods by graphene is directly carried out from FeOOH/GO colloids by taking advantage of an electrostatic self-assembly method, owing to the positively charged surface of FeOOH and the negatively charged surface of GO. This combination leads to multifunctional features of the electrode materials as follows: (1) An enhanced electrical conductivity makes the electrodes serve as the current collectors; (2) reinforced softness of the electrodes accommodates the large volume changes during charge–discharge cycles; (3) improved high specific surface area of the electrodes increases the accessibility of the active electrode materials to electrolyte;

(4) the pores formed by graphene and iron oxide particles facilitate ion transportation; and (5) iron oxide particles separate graphene and prevent their restacking or agglomeration and vice versa, thus improving the immersion and splitting of electrolyte into and out of the electroactive material. Consequently, the porous iron oxide/graphene hybrid nanocomposites deliver a good performance in the electrochemical energy storage. As expected, the incorporation of Fe_3O_4 in carbon matrix can greatly improve the electrochemical performance by inducing some vigorous redox reactions. Similarly, Kim et al. reported that composites of multi-walled carbon nanotubes and Fe_3O_4 exhibited specific capacitances of 165 F g^{-1} at a specific current of 0.2 A g^{-1} (Kim and Park 2011). The Fe_3O_4 and CNT together formed an interpenetrating network that provided a high specific capacitance and better cycling stability. An ultrathin nanoporous Fe_3O_4/carbon nanosheets with surface areas of 229 m^2 g^{-1} was reported by Liu et al.; the composite exhibited specific capacities of 163.4 F g^{-1} at a specific current of 1 A g^{-1}. An optimum Fe_3O_4 content in a Fe_3O_4/SiCF feeding ratio of 1.5:1 (SiCF/Fe_3O_4(1.5)) exhibited a high charge storage capacity, showing a specific capacitance of 423.2 F g^{-1} at a scan rate of 5 mV s^{-1} with a 81.8% rate performance from 5 to 500 mV s^{-1} in 1 M KOH aqueous electrolyte (Kim and Kim 2017). These results indicate the potential and advantages of iron-based materials for use as a high-energy and high power density supercapacitor electrode. Furthermore, an optimized electrochemical performance of electrode structures with proper control of the metal oxide/carbon was produced as shown in the scheme in Fig. 6.14. The morphology shows a hierarchical graphite

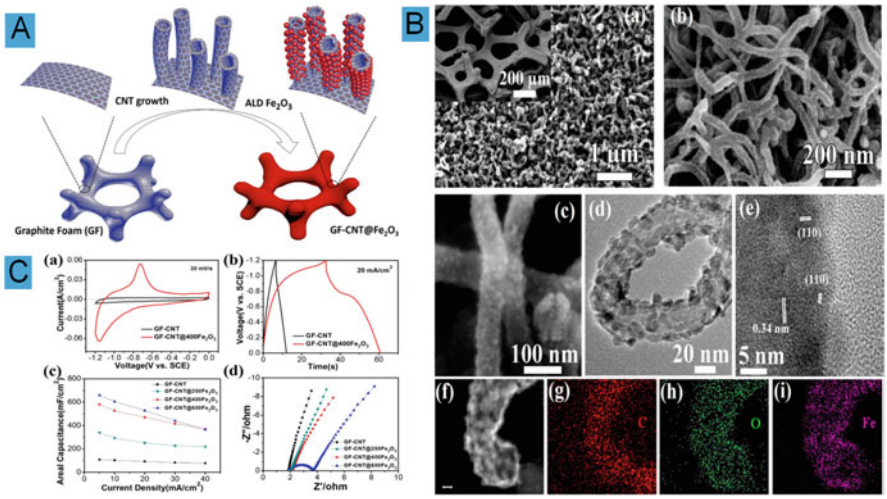

Fig. 6.14 (**a**) Schematic representation of the growth procedure of GF-CNT@Fe_2O_3 starting from graphite foam. (**b**) SEM and TEM characterization of GF-CNT@Fe_2O_3, (**a**–**c**) SEM and (**d**, **e**) HRTEM images of GF-CNT@Fe_2O_3, (f) HAADF-STEM image of a single CNT@Fe_2O_3 and (g–**i**) the corresponding STEM element mapping. The scale bar in (**f**) is 10 nm. (**c**) Electrochemical analysis, (**a**) CV curves and (**b**) charge-discharge curves of GF-CNT@400Fe_2O_3 and GF-CNT. (**c**) Rate properties and (**d**) EIS of four samples (With permission of Guan et al. 2015)

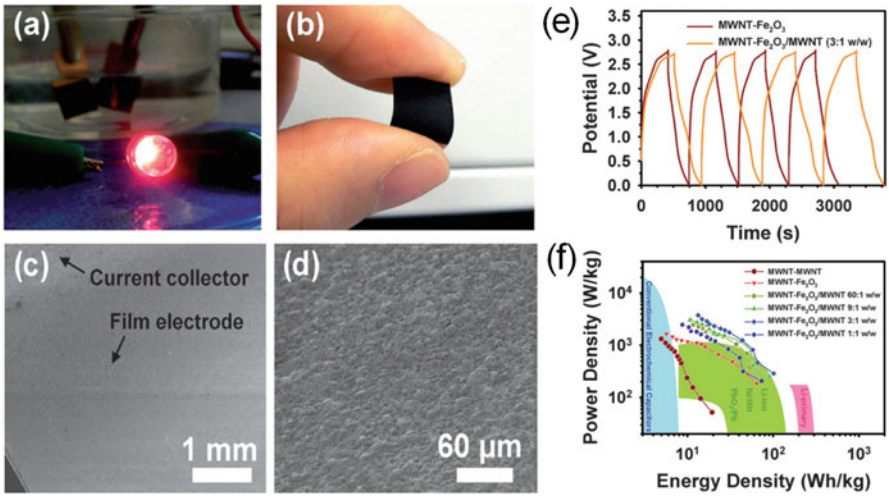

Fig. 6.15 (**a**) an optical image showing that a LED was lit brightly even after 300 cycles of the MWNT-α-Fe_2O_3/MWNT, (**b**) an optical image, (**c**, **d**) SEM images of the top surface of a α-Fe_2O_3/MWNT composite anode after 600 cycles and then bending, (**e**) galvanostatic charging/discharging behaviour of α-Fe_2O_3 and α-Fe_2O_3/MWNT composite as anode (MWNT as cathode) and (**f**) Ragone plot of MWNT cathode and various anode arrangements, together with other energy storage technologies (With permission of Zhao et al. 2009)

foam–carbon nanotube framework with thin layer of iron oxide coating on the surface to form (GF–CNT@Fe2O3) composite. Anode cells fabricated based on this material displayed a high energy of ~74.7 Wh/kg at a power of ~1400 W/kg and ~95.4% capacitance retention after 50,000 cycles of charge–discharge. This performance is superior to the results obtained by the GF-CNT alone and to many different forms of metal oxide-based supercapacitors, making it a promising candidate for the next generation of high-performance electrochemical energy storage.

Similarly, the spray deposition method was used for the fabrication of a flexible supercapacitor based on thin film of multi-walled carbon nanotube (MWNT) cathodes and hematite (α-Fe_2O_3)/MWNT composite anodes. The device fabricated provided a very high specific energy density of 50 Wh kg^{-1} at a power density of 1000 W kg^{-1} with potential window of 0–2.8 V, this energy value was eight times bigger than that fabricated for symmetric supercapacitors based on MWNT electrodes under the same conditions. The excellent performance of the hybrid devices was attributed to the incorporation of MWNTs into the α-Fe_2O_3 anodes, which leads to a decrease of internal resistance and an improvement in both the ion diffusion behaviour and the integrity of the α-Fe_2O_3 containing films (Zhao et al. 2009) (Fig. 6.15).

6.1.2.4 Vanadium Oxide (V_2O_5)

Vanadium oxide is gaining considerable research interest as suitable electrodes for supercapacitor owing to their low cost, layered structure and its ability to exist in variable oxidation states (e.g. V_2O_5, V_2O_3 and V_4O_7) (Wei et al. 2012; Saravanakumar et al. 2012; Li et al. 2013; Cao et al. 2014). The electronic structure, charge density, transport properties and phase transitions of different vanadium oxides are expected to vary with the composition. Vanadium pentoxide, V_2O_5, possesses the unique advantages of high-energy density (Yang et al. 2011b), and wide potential window arising from its variable oxidation states (Choi et al. 2006) makes it suitable as electrode material for supercapacitors. Different nanostructures of V_2O_5 such as nanowires (Wang et al. 2015), nanotubes (Yu et al. 2012), nanorods (Tien and Chen 2013), nanofibers (Wee et al. 2010), hollow spheres (Yang et al. 2013) and V_2O_5 nanosheets constructing 3D architectures (Xiong et al. 2008) have been synthesized using techniques such as hydrothermal (Xiong et al. 2008), electrospining (Wee et al. 2010; Yu et al. 2011), template-assisted growth (Cheng et al. 2008) and various other methods are used to produce these unique nanostructures. For example, Zhang et al. (Zhang et al. 2016b) reported three different structures of V_2O_5 (nanobelts, nanoparticles and microspheres) by a simple hydrothermal route, and the combination of calcination and the electrochemical results obtained indicate that microspheres lead to a significant improvement of storage capacity with a specific capacitance of 308 F g^{-1} in 1.0 M $LiNO_3$ electrolyte. Figure 6.16 shows the processing of bulk V_2O_5 into nanosheets of V_2O_5 of 4 nm and lateral dimension of up to micrometres via hydrothermal system and characterized with the various state-of-the-art facilities such as TEM, SEM and STEM (Fig. 6.16b). The active electrode material displayed excellent specific capacitance of 451 F g^{-1} in a neutral aqueous Na_2SO_4 electrolyte, as the 3D architectures are utilized for energy storage, with capacitance retention after 4000 cycles is more than 90%, and the energy density is up to 107 W·h·kg^{-1} at a high power density of 9.4 kW kg^{-1} (Zhu et al. 2013). The performance was due to the unique 3D V_2O_5 architecture that provides high surface area for enhanced electrolyte/electrode interaction and also reduces the diffusion path both for electrons and ions.

Nanoporous V_2O_5 network was prepared via a capping agent-assisted technique and examined the effect of annealing on the morphology, electrochemical and structural properties (Saravanakumar et al. 2012). The electrode fabricated exhibited a specific capacitance of 316 F g^{-1}, which is attributed to the creation of facile nanochannels for ion diffusion and facilitates the easy accessibility of ions. Nevertheless, despite the high capacitance values recorded for V_2O_5 nanostructures, their poor electronic conductivity and high dissolution issues in liquid electrolyte due to phase changes upon cycling, which gradually erodes the quantity of electrochemically active materials, are detrimental to high-rate, long-term cycling and mechanical stability (Qu et al. 2012). Thus, the combination of V_2O_5 with carbon-based material or doping of the V_2O_5 has been demonstrated to be an effective strategy to improve electronic transport (Chen et al. 2009, 2011b). As such, various composites have

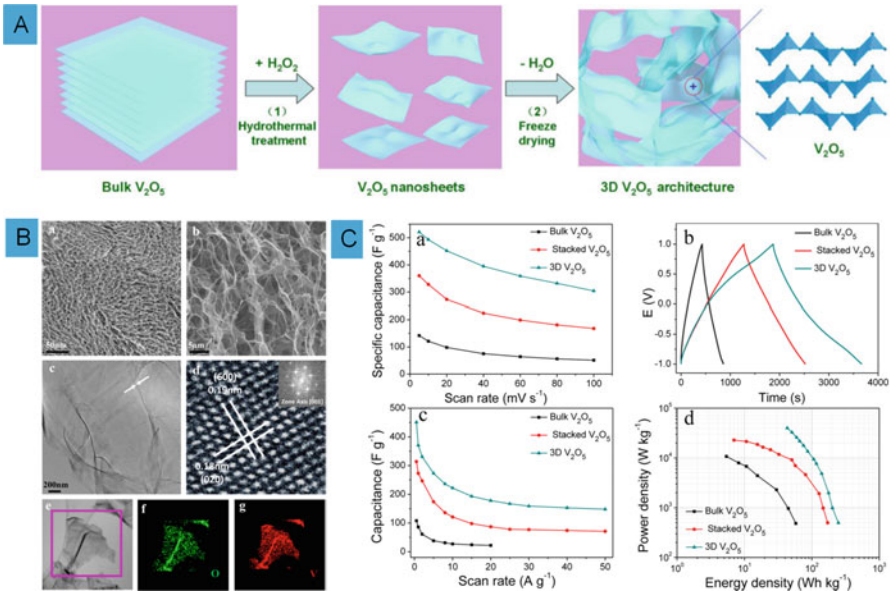

Fig. 6.16 (**a**) Schematics of the fabrication steps of the 3D V_2O_5 architectures: (1) producing thin and flexible V_2O_5 nanosheets via the hydrothermal treatment of V_2O_5 powder with H_2O_2 at 190 °C; (2) removal of water from the as-prepared V_2O_5 nanosheet samples via freeze-drying. (B) Characterization of the 3D V_2O_5 constructs, (**a**, **b**) FESEM; (**c**, **d**) TEM images (FFT, inset); (**e**–**g**) STEM image and corresponding elemental mapping of (**f**) oxygen and (**g**) vanadium. (**c**) Electrochemical performance of 3D V_2O_5 (**a**) Specific capacitances from CV. (**b**) Galvanostatic charge/discharge (GCD) at a specific current of 0.5 A·g^{-1}. (**c**) Specific capacitances from GCD (With permission of Zhu et al. 2013)

been investigated, for example, W-doped V_2O_5 nanobelts were prepared and exhibited specific capacitance of 407 F g^{-1} at 0.5 A g^{-1}. Similarly, V_2O_5/reduced graphene oxide (rGO) hybrid nanostructures are fabricated and showed a higher specific capacitance (484 F g^{-1} at 0.5 A g^{-1}), rate capacity (251 Fg^{-1} at 10 A g^{-1}) and cyclic stability (83% up to 1000 cycles) (Saravanakumar et al. 2016). The improved capacitive performance was due to the high conductivity of rGO and electrochemical activity of V_2O_5. Similarly, an effective facile electrochemical oxidation method was reported to significantly boost the durability and capacitance of VO_x through tuning the valence state of vanadium (Yu et al. 2015). Figure 6.17 shows the SEM, TEM and the electrochemical performance of V_2O_3 nanorods. The valence state of vanadium is optimized through a very facile electrochemical oxidation method, with morphological characterization revealing porous tubular structures (Fig. 6.17a, b). A superior electrochemical performance with rectangular cyclic voltammograms (Fig. 6.17c) and a long stability after 100,000 cycles (Fig. 6.17h) for the prepared electrodes was demonstrated with an in-depth study on the variation for the valence state of vanadium during the oxidation process, and the cyclic

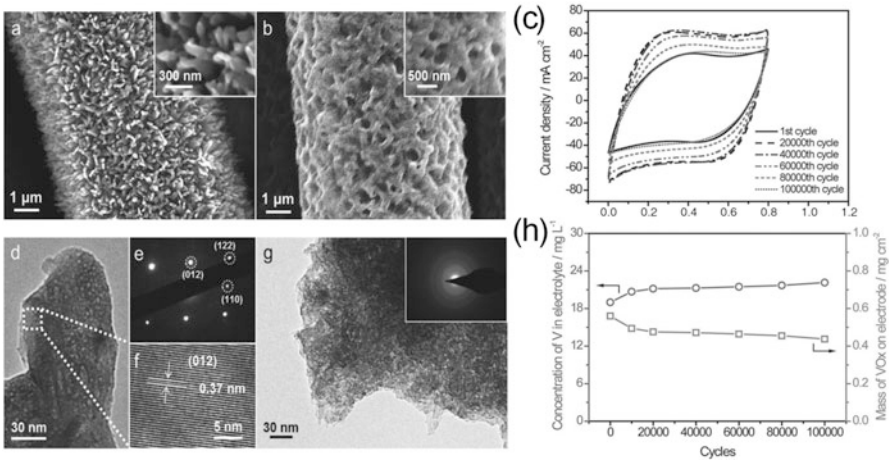

Fig. 6.17 SEM images of as-prepared (**a**) V_2O_3 and (**b**) VO_x samples. (**c**) CV curves collected at 100 mV s^{-1} of VO_x electrode after different cycles. (**d**) TEM image, (**e**) SAED pattern, and (**f**) HRTEM images of a V_2O_3 nanorods. (**g**) TEM image and corresponding SAED pattern of a VO_x sample. (**h**) The concentration of V element in the electrolyte and the mass loading of active materials remained in electrode after different cycles (With permission of Yu et al. 2015)

stability indicates that the long cyclic stability has an important relationship with the distribution of the valence state of vanadium (Yu et al. 2015).

The electrochemical co-deposition of vanadium oxide and polypyrrole was also explored for high-performance supercapacitor devices as shown in Fig. 6.18. The V_2O_5–PPy composite exhibited fibre-like morphology (Fig. 6.18a), and due to the organic-inorganic synergistic effect, the composite exhibits good charge storage properties with a large potential window from −1.4 to 0.6 V vs SCE in a three-electrode configuration, exhibiting a specific capacitance of 412 F g^{-1} at 4.5 mA cm^{-2} (Fig. 6.18b) with good capacitance retention as shown in Fig. 6.18c. The device assembled based on this V_2O_5–PPy composite displayed a high operating voltage of 2 V and a high energy density of 82 Wh kg^{-1} (at the power density of 800 W kg^{-1}) (Bai et al. 2014). The results demonstrate the development of vanadium-based electrode materials as a low-cost strategy towards the advancement of high-performance supercapacitors.

Similarly, VO and VO_2 have also been explored and have demonstrated excellent results, for example, VO coupled with amorphous vanadium covalent bonds (VO_x) was incorporated into carbon nanofibres (VO/VOx/CNF) by electrospinning and heat treatment. The VO/VOx/CNF electrode displayed specific capacitance of 325.7 F g^{-1} at a specific current of 1 A g^{-1} and maintaining 92% of its initial capacitance after 5000 cycles at a specific current of 4 A g^{-1} in a 6 M KOH. The superior electrochemical performance of VO/VOx/CNF was attributed for two reasons, namely, the enhanced conductivity brought upon the incorporation of quasi-metallic VO ($\sim$ 102 Ω^{-1} cm^{-1}) and the network of nanowire and secondly the rapid ion transfer rate caused by the rich vanadium redox couples VO/VOx as

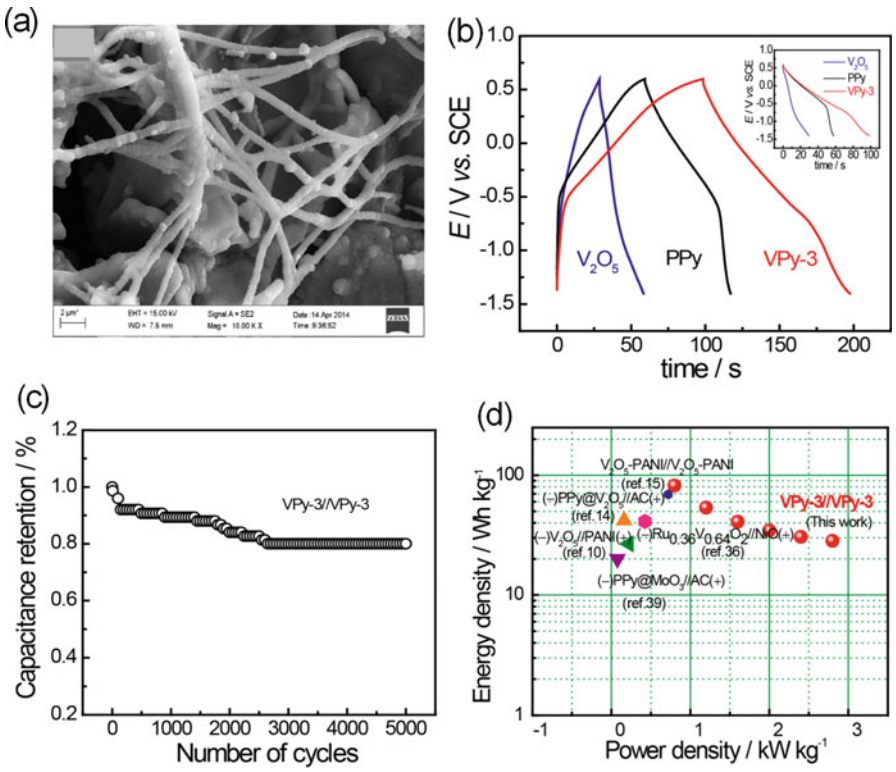

Fig. 6.18 (**a**) SEM images of VPy-3 deposited on carbon cloth substrate, (**b**) galvanostatic charge−discharge profiles of VPy-3, V_2O_5 and PPy collected at a specific current of 4.5 mA cm^{-2}, (**c**) cycling stability of VPy-3//VPy-3 collected by galvanostatic charge−discharge experiments at a specific current of 9 mA cm^{-2} and (**d**) Ragone plots of VPy-3//VPy-3, the values reported for other supercapacitors are included for comparison (With permission of Bai et al. 2014)

well as the developed pore structure (Tang et al. 2016). VO_2 has also been studied as a potential electrode material for supercapacitors, and they have shown a great promise for potential application (Yan et al. 2016), for example, Rakhi et al. reported VO_2 nanosheet electrodes in organic gel electrolyte for supercapacitor applications by hydrothermal method, and the electrodes exhibited a specific capacitance of 405 F g^{-1} at a specific current of 1 A g^{-1} (Rakhi et al. 2016). Also, Deng et al. prepared hybrid of graphene/VO_2 (RG/VO_2) for supercapacitors by hydrothermal reduction method, and the material exhibited a specific capacitance of 225 F g^{-1} at a specific current of 0.25 A g^{-1} in 0.5 MK_2SO_4 aqueous solution (Deng et al. 2013).

6.1.2.5 Tin Oxide (SnO_2)

Tin oxide, SnO_2, is an n-type wide band gap semiconducting material not only with the direct band gap energy of 3.5–3.9 eV (Spence 1967; Arlinghaus 1974) but also with the indirect band gap energy of around 2.6 eV (Kawasaki et al. 1970). The SnO_2 possess the advantages of being inexpensive, efficient semiconducting in nature, environmentally safe, high electrical and optical properties and high chemical stability. These properties have made SnO_2 to be widely explored in many applications such as electrochemical sensors, transistors, catalysts, energy storage and conversions (Yan et al. 2010; Chen et al. 2011a; Zhang et al. 2011; Hou et al. 2013). The interest in the electrochemical energy storage such as SCs and batteries is due to its relative abundance, high theoretical specific capacity (782 mAh g^{-1}) and chemical stability (Tang et al. 2013).

The nanostructures of SnO_2 can also be synthesized via different techniques such as pulsed laser deposition (Pham et al. 2014), co-precipitation (Du et al. 2012), SILAR (Yıldırım et al. 2012), chemical bath deposition (Pusawale et al. 2013), electrodeposition (Yang et al. 2011a), hydrothermal (Hui-Chi Chiu 2007) and thermal evaporation (Kim et al. 2006). The SnO_2 nanoparticles synthesized by co-precipitation technique were evaluated and tested for SC application and displayed a maximum specific capacitance of 122 F g^{-1} at a scan rate of 2 mV s^{-1} (Manikandan et al. 2016). Hierarchical SnO_2 nanostructures (HTNs) prepared by hydrothermal method and characterized revealed a crystalline tetragonal rutile structure of SnO_2 as shown in Fig. 6.18 (Liu et al. 2014). The morphologies of the prepared SnO_2 revealed hierarchical flower shapes in very high density (Fig. 6.18b). The typical diameter of a single hierarchical flower-shaped morphology was $\sim 3 \pm 1$ μm. It was also observed that the hierarchical flower-shaped structures are made of ultrathin nanosheets of ~20 nm in size, which intermingled with each other leading to triangular nanostructures. The HRTEM images (Fig. 6.18e, f) show well defined lattice fringes with lattice spacing of 0.337 and 0.265 nm, corresponding to the (110) and (101) lattice planes of SnO_2, respectively. The SAED pattern shown as inset confirmed the prepared SnO_2 nanosheet crystalline. The electrochemical performance of the SnO_2 structures was evaluated in three-electrode configuration using 1 M Na_2SO_4 aqueous electrolyte. A specific capacitance of 187.7 F g^{-1} was obtained at a specific current of 1 A g^{-1} and was attributed to the hierarchical nature and thin thickness of the nanosheets. Semiconductor quantum dots (QDs) play a vital role in technological and biological applications; SnO_2 QDs exhibit a typical behaviour in comparison with their bulk counterparts due to high surface to volume ratio and excitonic confinement effects (Chen et al. 2005, 2011b). Thus, it is important to understand this distinct nature of QDs such that it can be used more effectively in applications. Bonu et al. carried out electrochemical supercapacitor performance of SnO_2 quantum dots, and it was shown that (QDs) can significantly improve the understanding on the reasons behind the better performance, and it will also help in using QDs or smaller size nanoparticles (NPs) more efficiently in supercapacitors (Bonu et al. 2016). The specific capacitance of the stable SnO_2 QDs showed only 9%

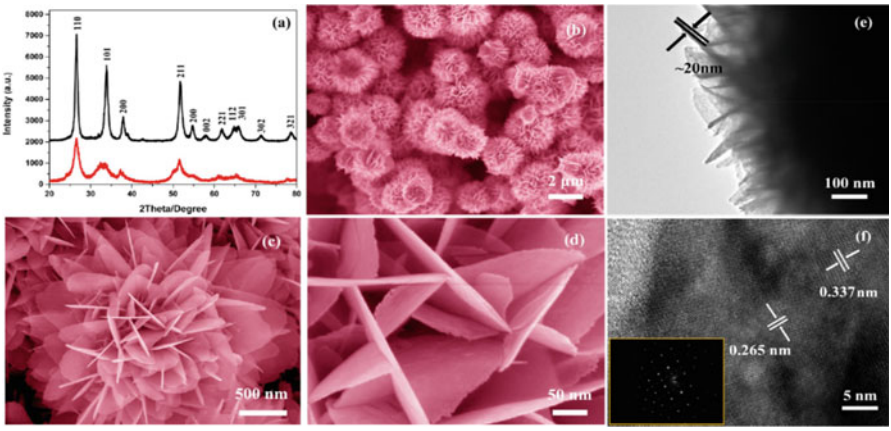

Fig. 6.19 XRD patterns of the prepared SnO_2 nanostructures before (red line) and after calcination (black line); (**b**–**d**) FESEM images, (**e**) low-magnification TEM image and (**f**) high-resolution TEM (HRTEM) image of the prepared hierarchical SnO_2 nanostructures. Inset in (**f**) exhibits the typical corresponding SAED pattern (With permission of Liu et al. 2014)

loss while increasing the scan rate from 20 to 500 mV/S, and the capacitance loss for the QDs is less than 2% after 1000 cycles of charging/discharging, whereas for the 25 nm SnO_2 NPs, the capacitance loss is 8% after 1000 cycles. The new findings about the SnO_2 QDs can be helpful supercapacitors (Fig. 6.19).

Velmurugan et al. (2016) further studied graphene-doped SnO_2 and showed the overall specific capacitance of the composite electrode (SnO_2/graphene) corresponds to the combined contribution from electrochemical double-layer charging and pseudocapacitive behaviour of the composite. The resultant specific capacitance was 50 F g^{-1} for the pristine SnO_2 and 100 F g^{-1} for SnO_2/graphene composite at a high scan rate of 50 mV s^{-1}. The specific capacitance of 470 and 818 F g^{-1} was obtained at low scan rates. A pulse microwave-assisted deposition technique was also explored to grow SnO_2 crystals with homogeneously distribution on rGO sheets to form a composite of SnO_2/rGO composites as shown in Fig. 6.20.

The specific capacitance of the devices fabricated from the composite exhibited specific capacitance of 348 F g^{-1} at a specific current of 50 mA g^{-1}, maximum energy density of 32.2 Wh kg^{-1} with a power density of 1000 W kg^{-1}. The improved capacitance and energy values were attributed to the fact that the SnO_2 crystals not only serve as spacers to create more active sites on the rGO surface but also maximized the fraction of hydrophilic surface, which is more accessible for the formation of the electric double layer (Hsieh et al. 2014). Similarly, SnO_2 was also decorated onto Ti_3C_2 by an efficient and simple microwave irradiation method to form SnO_2-Ti_3C_2 nanocomposite. Figure 6.21a–c showed the layered structure of the Ti_3C_2 with the SnO_2 intercalated into the layer of the Ti_3C_2 to prevent stacking of the layers. The composite exhibited an ideal capacitive behaviour from the CV at different scan rates and GCD at different specific current densities presented in Fig. 6.21d, e. The high specific capacitance of 126 F g^{-1} at 1 A g^{-1} and 100 F g^{-1}

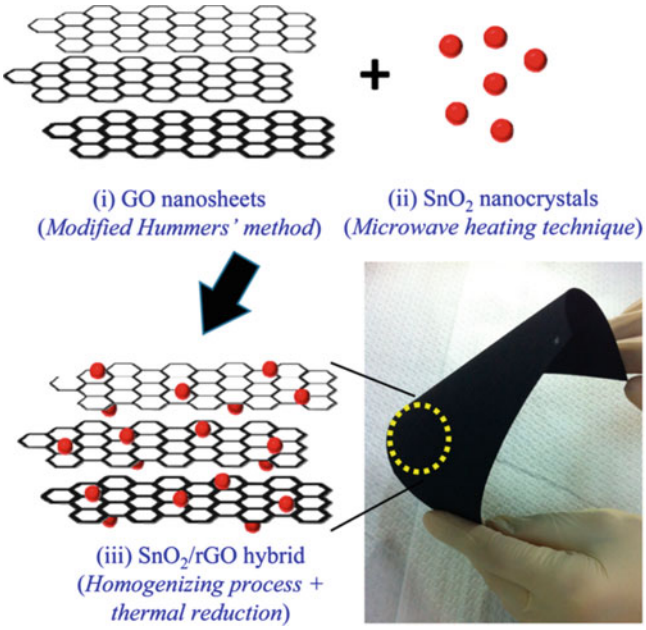

Fig. 6.20 Schematic diagram for growing SnO_2/rGO composites through the following steps: (i) GO sheets by the Hummers' method, (ii) SnO_2 nanocrystals by microwave heating technique and (iii) homogenizing dispersion and thermal reduction. The bottom right photo shows as-prepared flexible SnO_2/rGO CP electrode sheets (With permission of Hsieh et al. 2014)

at 10 A g^{-1} specific current was obtained for the composite. The composite material showed an improved electrochemical performance compared to its precursors (Fig. 6.21f). The composites retained almost 82% of its initial capacitance after 8000 cycles at a specific current of 3 A g^{-1} (Fig. 6.21g). The improved performance observed was due to the intercalation of the Sn^{2+} into the layers of the Ti_3C_2 and also prevent the stacking of Ti_3C_2 layer (Zheng et al. 2017).

6.1.2.6 Tungsten Oxide (W_xO_y)

Tungsten trioxide (WO_3) semiconductor having an indirect band gap of 2.5–2.8 eV has also emerged as a promising material for electrochemical applications due to its low cost, high electrical conductivity, good chemical stability in acidic aqueous solution and high theoretical capacity (Zheng et al. 2011). The interest for this material in electrochemical energy storage is due to its efficient charge storage/delivery dynamic and its reversible valence change (i.e. change of oxidation state between W^{6+} and W^{5+} centres) (Deb 2008; Zheng et al. 2011). Pseudocapacitive charge storage behaviour in highly conductive ordered mesoporous tungsten oxide electrodes was reported by Jo et al. (2011). They observed a voltage rise of the m-WO_{3-X} electrode, which is similar to the EDLC, displayed a high rate capability,

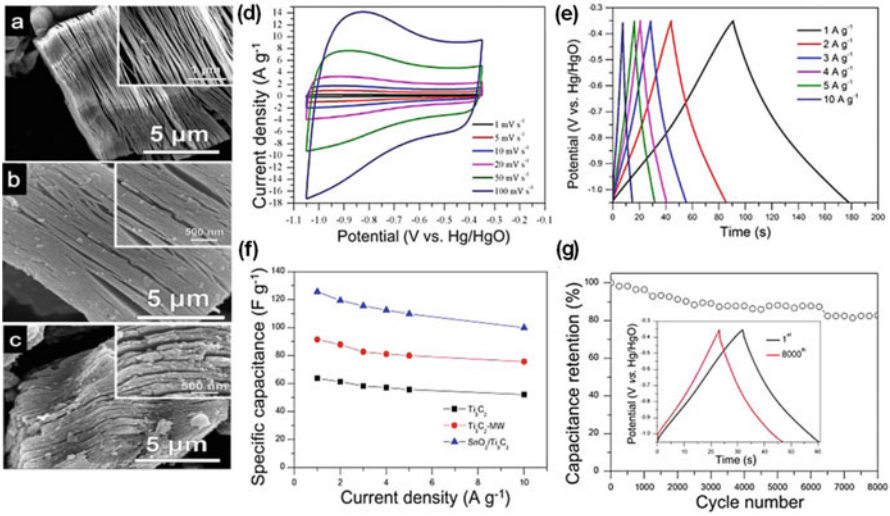

Fig. 6.21 SEM images for (**a**) Ti_3C_2, (**b**) Ti_3C_2-MW and (**c**) SnO_2-Ti_3C_2, (**d**) CV curves of SnO_2-Ti_3C_2 electrode at various scan rates, (**e**) GCD curves of SnO_2-Ti_3C_2 electrodes, (**f**) the plots of the specific capacitance of the three electrodes under different specific current and (**g**) capacitance retention (the inset shows charge-discharge curves before and after 8000 cycles), of SnO_2-Ti_3C_2 electrode after 8000 GCD cycles at 3 A g^{-1} (With permission of Zheng et al. 2017)

which was attributed to its fast proton diffusion within the metal oxide wall and the short path of electrolyte transport through the well-ordered mesopores. Thus, the proposed Fig. 6.22 explained the possible mechanism in the m-WO_{3-X} electrode.

As shown in Fig. 6.22, the three phases within the WO_{3-X} wall were separated. The tungsten metal has two oxidation states of W^{5+} and W^{6+}, and the proton is obtained from the electrolyte phase (Jo et al. 2011). An interphase is assumed to exist between electrode and electrolyte, where the faradaic reaction takes place. Using a simple calculation to estimate the total charge (q*t = 67 C g^{-1}) in cyclic voltammetry (CV) measurement, leads to a charge utilization of 15,533 C mol^{-1}(67 C g^{-1} X 231.84 g mol^{-1}), which indicated that only 16% of W atoms of the m-WO_{3-X} electrode. When the electrode potential increases to 0.6 V, most of the W^{5+} species oxidizes to the W^{6+} state. This oxidation state leads to a decrease in the conductivity, and the charge transfer resistance (R_{ct}) becomes larger. When the potential is lowered to 0 V, the state of the interphase is reduced to W^{5+} and also leads to an increase in the electrical conductivity (lower resistance) of the electrodes. However, WO_3 is suitable as a negative electrode material, and recently, Qiu's group reported the flower-like nanostructures of WO_3 as negative electrode in solid-state asymmetric supercapacitors and exhibited a specific capacitance of 196 F g^{-1} at a scan rate of 10 mV s^{-1} (Qiu et al. 2016). Upadhyay et al. synthesized nanochannel layers of WO_3 by electrochemical anodization in orthophosphoric acid (o-H_3PO_4) (Upadhyay et al. 2017). The cross-sectional SEM images (Fig. 6.23a–c) show nanochannel layers of WO_3.

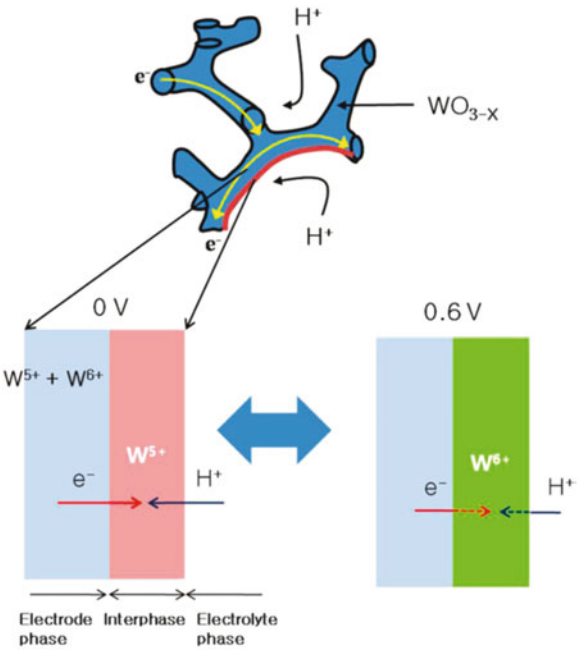

Fig. 6.22 Schematic illustration of the pseudocapacitive charge storage mechanism in the m-WO_{3-X} electrode. Upper part is for the schematic transport of electron and proton within m-WO_{3-X}. Bottom part indicates a schematic change of the oxidation state during pseudocapacitive charging/discharging. Note that transports of electron (e^-) and proton (H^+) within the interphase at 0 V became sluggish at 0.6 V vs Ag/AgCl (With permission of Jo et al. 2011)

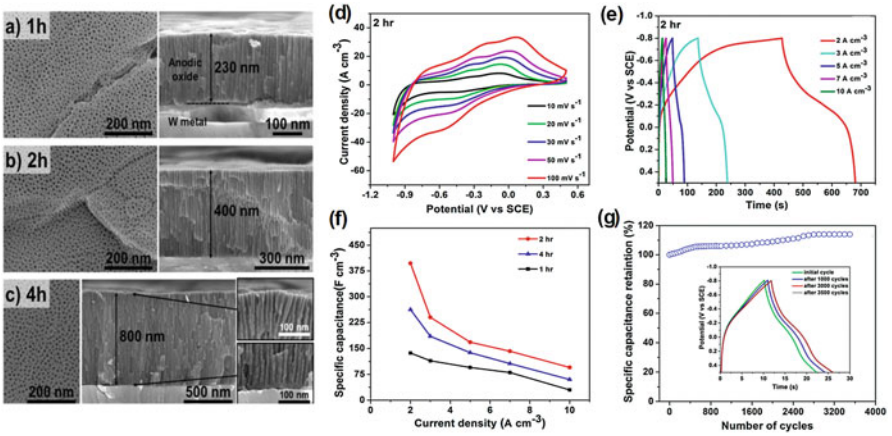

Fig. 6.23 (**a**–**c**) Top-view (left) and cross-sectional(right) SEM images of WO3 nanochannel layers formed by self-organizing electrochemical anodization of W foils in pure hot H_3PO_4 (100 C 5 V) for different times: (**a**) 1 h, (**b**) 2 h and (**c**) 4 h, (**d**–**e**) CV and galvanostatic charge-discharge plot of 2 h. anodized sample at different scan rates and current densities, respectively, (**f**) specific capacitance vs. current densities for all the samples and (**g**) capacitance retention up to 3500 cycles at 10 A cm^{-3} (inset: charge discharge plots over time). All the experiments were performed with annealed sample (450 C, air, 1 h) (With permission of Upadhyay et al. 2017)

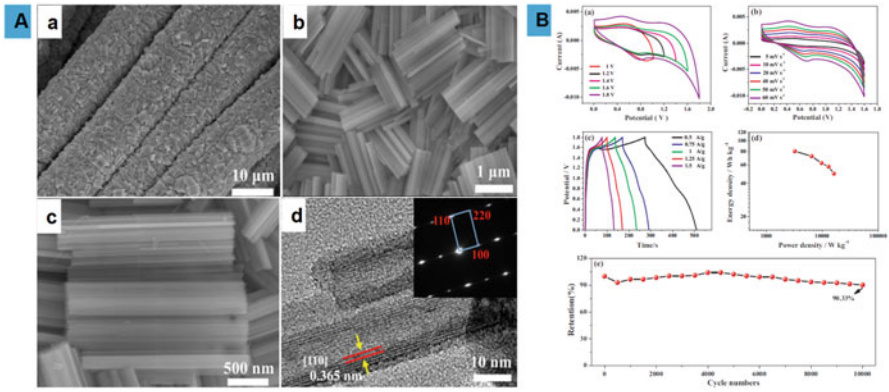

Fig. 6.24 (**a**) SEM and TEM images, (**a**)–(**c**) SEM images of the as-prepared product of WO_3 nanotube bundle, (**d**) the corresponding HRTEM image. (**b**) Electrochemical analysis: (**a**) CV curves in different potential windows at 60 mV s^{-1}, (**b**) CV curves of the as-fabricated ASC device at various scan rates from 5 to 60 mV/s in 1.8 V potential window, (**c**) galvanostatic charging/discharging curves of ASC device at different current densities, (**d**) Ragone plots of ASC device and (**e**) cycling performance at constant specific current of 5 A/g (With permission from Wu and Yao 2017)

The top surface of the layers is homogeneous and shows the open pores, with inner diameter of ca. 10 nm. The cross-sectional SEM images (right) show clearly that the anodic WO_3 has a nanochannel structure, with aligned vertically oriented channels that extend from the top surface of the anodic film to the oxide-metal interface. These channels are open at the top surface and remain open (with inner diameter of ca. 10 nm) across the entire channel length, regardless of the anodic oxide thickness. These layers show remarkable pseudocapacitive behaviour within the potential window of −0.8–0.5 V in 1 M Na_2SO_4 as shown in Fig. 6.23d–g.

A higher capacitance was obtained for the WO_3 structures grown for 2 h when compared to the other samples, i.e. 397 F cm^{-3} at 2 A cm^{-3} in a potential range of 1.3 V, and displayed an excellent capacitance retention up to 3500 cycles at 10 A cm^{-3} as shown in Fig. 6.23g. The cyclic stability showed that the returned 27% of the total capacitance originated from surface adsorption/desorption process, while the remaining 73% originated from a diffusion-controlled process. The WO_3 nanotube bundles made by Wu and co-workers (Wu and Yao 2017) and used as a negative electrode in an asymmetric device against PANI as a positive electrode. As shown in Fig. 6.24a (a–d), the SEM and TEM images revealed the bundles of the WO_3 nanotubes, and the electrochemical performance of the assembled pseudocapacitor device (Fig. 6.24b (a–e) showed that this electrode material could be a potential candidate in energy storage application.

An area capacitance of 2575.3 mF cm^{-2} at a specific current of 3 mA cm^{-2} and a specific capacitance of 615.7 F g^{-1} at a specific current of 1 A g^{-1} were obtained in a three-electrode configuration, respectively. The asymmetrical device fabricated displayed a wide voltage window of 1.8 V from the CV and GCD presented in

Fig. 6.24b (c). A high energy densities of 80.1 W h kg^{-1} and 49.5 W h kg^{-1} were obtained at power densities of 3240 W kg^{-1} and 16,200 W kg^{-1}, respectively.

6.1.2.7 Bismuth Oxide (Bi_xO_y)

Bismuth oxide, Bi_2O_3, also exhibits intrinsic properties such as refractive index, energy bandgap (2.8 eV), dielectric constant and photoconductivity similar to many semiconductors. This metal oxide is suitable for large-range applications such as sensors, catalysis, energy storage and conversion. Recently, this metal oxide has emerged as good electrode material for energy storage applications in SCs due to its high theoretical capacity (690 mAh g^{-1} and 6280 mAh cm^{-3}) and electrochemical stability (Gujar et al. 2006; Liu et al. 2012, 2015b). The structure of the Bi_2O_3 can be described as a sequence of alternating layers of bismuth atoms parallel to the (100) plane of the cell and oxide ions in the c-axis direction (Michel Drache et al. 2007). The electrode made up of Bi_2O_3 thin film grown on copper substrates at room temperature via electrodeposition from an aqueous alkaline nitrate has been fabricated and tested for supercapacitor application by Gujar et al. (2006). The supercapacitor device made from this electrode displayed good electrochemical performance and durability, with specific capacitance of 98 F g^{-1} reported. Similarly, electrode potential oscillations have been used for the synthesis of hierarchical rippled Bi_2O_3 nanobelts, and the electrodes fabricated exhibited excellent stability and electrochemical performance (Zheng et al. 2010). Based on the reported electrochemical energy storage capabilities of Bi_2O_3, there is no doubt that this material has potential for application in SCs. Nevertheless, this metal oxide still suffers from low abundance and poor conductivity and rate capability, thus limiting its application. Due to the mentioned challenges, researchers have explored the use of carbon-based materials with Bi_2O_3 either in composite form or in asymmetric configuration to improve the electrochemical performance of the SC device taking advantage of the properties offered by both materials. Senthilkumar et al. (2014) fabricated asymmetric device based on Bi_2O_3 and activated carbon (AC) in redox additive aqueous electrolyte and achieved remarkable energy density of 35.4 Wh kg^{-1} (Senthilkumar et al. 2014). Ng and co-workers studied Bi_2O_3 temperature effects in a bismuth oxide/manganese oxide (Bi_2O_3/MnO_2) SCs. An improved electrochemical performance was achieved judging from the CV curves shown in Fig. 6.25 for the Bi_2O_3 measured at 60 °C displaying larger area compared to those at 30 and 0 °C, which corresponds to a high specific capacitance of 150.2 F g^{-1} at a scan rate of 2 mV s^{-1}. The increase in capacitance was attributed to the enhanced ion mobility at elevated temperature, which prompted greater charge transfer and storage capability. Furthermore, the evaporation of electrolyte at a high temperature could induce the physisorption of electrolyte ions and give rise to faradaic currents, which enhanced the capacitance performance. The GCD also shown in Fig. 6.25 displayed evidence that the application of temperature stimulated electrochemical activation, leading to high capacitance performance compared to that at 0 °C. The linear voltage−time profiles at 60 °C compared to those at 30 and 0 °C from the prolonged discharge time

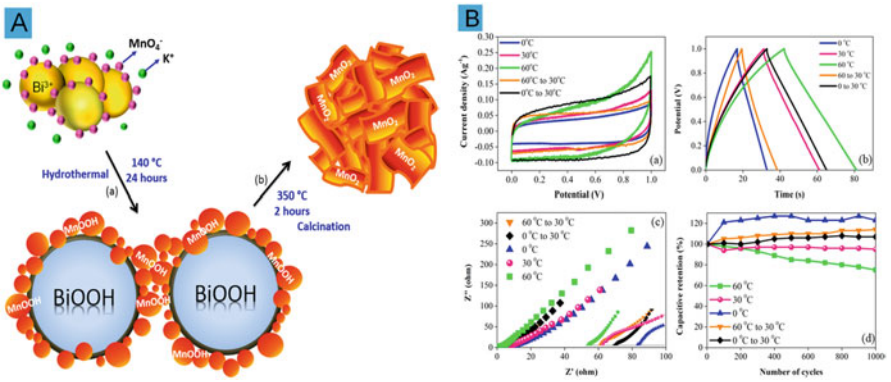

Fig. 6.25 (**a**) Schematic representation of the plausible growth mechanism of Bi_2O_3/MnO_2 on nickel foam substrate during hydrothermal process. (**b**) Electrochemical analysis: (**a**) Cyclic voltammogram, (**b**) galvanostatic charge/discharge, (**c**) Nyquist plot and (**d**) life cycle of Bi_2O_3/MnO_2 supercapacitors at different temperatures. Inset shows the magnified EIS spectra of Bi_2O_3/MnO_2 supercapacitors at different temperatures (With permission of Ng et al. 2018)

indicated a good capacitive behaviour and better charge storage capability at elevated temperature. An energy and power densities of 9.5 Wh kg^{-1} and 102.6 W kg^{-1} were obtained at 60 °C, respectively, which shows a great improvement to values obtained at 0 °C and 30 °C. The Nyquist plot (Fig. 6.25c) shows a slightly higher resistance at 0 °C than that at 30 and lower resistance values at 60 °C which is believed to be due to the expansion of the matrix, which facilitated the diffusion of electrolyte ions. Moreover, the SC device achieved energy densities of 4.9 and 6.9 Wh kg^{-1} and power densities of 53.8 and 74.8 W kg^{-1} at 0 and 30 °C, respectively. The Bi_2O_3/MnO_2 composite exhibited a superior stability retaining 95% of the original capacitance at 30 °C and > 75% at the high temperature of 60 °C (Ng et al. 2018).

The synergistic effect between the Bi_2O_3 and MnO_2 materials enhanced the electrochemical performances of the composite electrodes and dramatically improved the cyclic reversibility, sustainability and stability of the Bi_2O_3/MnO_2 supercapacitor, regardless of the temperature influence. These results showed that the device with a longer defrosting period possessed better electrolyte ion diffusivity, which therefore leads to enhanced capacitive performances and show that the Bi_2O_3 is suitable for use in the automotive sector.

6.1.2.8 Indium Oxide (In_2O_3)

Nanostructured In_2O_3, a transparent conductive oxide with a wide bandgap (Eg∼3.65 eV), has recently attracted attention due to its high electrical conductivity, high optical transmittance and excellent luminescence. Because of these fascinating properties, In_2O_3 has been used for applications such as antireflection coatings

(Wang et al. 2016b), gas sensors (Zheng et al. 2015), lithium–ion batteries (Osiak et al. 2013) and supercapacitors (Bastakoti et al. 2013) and has been produced using different methods such as spray pyrolysis (Korotcenkov et al. 2002), chemical vapour deposition (CVD) (Tuzluca et al. 2017), pulsed laser deposition (PLD), thermal evaporation (Liu et al. 2015a), carbothermal methods (Huang et al. 2007) and hydrothermal synthesis (Padmanathan et al. 2016). The interest in electrochemical capacitors is based on the reversible reaction below (equation xx) which gives rise to high theoretical specific capacity ~580 mAh g^{-1}.

$$\mathrm{In} + \mathrm{xLi}^{+} + \mathrm{xe}^{-} \leftrightarrow \mathrm{Li}_x\mathrm{In}\ (0 \leq x \leq 3) \tag{6.12}$$

The In_2O_3 nanostructures can exhibit different morphologies, which are suitable as electrodes for materials for supercapacitors. For example, 1-D single crystal In_2O_3 nanotowers, nanobouquets, nanocones and nanowires were synthesized using the CVD system over different temperature regions (1000, 900, 800, 700 and 600 °C) as shown in Fig. 6.26. The interests of this work displayed the relationship between the size and shape of In_2O_3 nanostructures to the electrochemical properties. The synthesized materials were explored as electrodes for electrochemical capacitors, and the In_2O_3 nanowires displayed the highest areal capacitance of 16.6 mF cm^{-2} with cycle stability of 66.8% after 10,000 cycles (Tuzluca et al. 2018). The morphology of these various shapes of In_2O_3 nanostructures indicated on FESEM image and line scanning and point EDS analyses of the sample, attesting that nanobouquets had In and O atoms at their main trunks and tips, are shown in Fig. 6.26. As it was also shown, the absence of Au at the tips of nanobouquets designates that the growth mechanism of these nanobouquets is via the growth path rather than the VLS growth pathway.

The electrochemical performance of the In_2O_3 nanostructure presented in Fig. 6.27 displayed the highest areal capacitance value obtained from In_2O_3 nanowires due to the fact that the nanoscale wires have high surface area to volume ratio compared to the nanostructures. The observed result is because electrode materials with nanowire morphology have a higher capacitance and amount of charge storage. It is known that the increase in surface area of an electrode makes ionic diffusion paths to become shorter during reactions due to the synergistic effect arising from both the electrode and electrolyte. Thus, electrode materials with nanowire morphology can increase the electrochemical performance of supercapacitors. The CV and GCD curves (Fig. 6.27b, c) taken in the potential range of 0–0.8 V and 0 to (−0.6) V, respectively, indicated the electrochemical behaviour similar to the ones observed in the literature. Figure 6.27b shows the CV curves of the sample and the bare Si substrate at 10 mV s^{-1} scan rate. An areal capacitance values of 10.1, 5.7, 4.2 and 3.7 mF cm^{-2} were obtained for sample A (nanotowers); 6.7, 4.5, 3.5 and 3 mF cm^{-2} for sample B (nanotowers); 12.5, 10.8, 9.6 and 8.2 mF cm^{-2} for sample C (nanobouquets); 4.9, 4.1, 3 and 2.7 mF cm^{-2} for sample D (nanocones); and 16.6, 14, 12.3 and 11.3 mF cm^{-2} for sample E (nanowires) (Fig. 6.27d) at a specific current of 0.04, 0.06, 0.08 and 0.1 mA cm^{-2}.

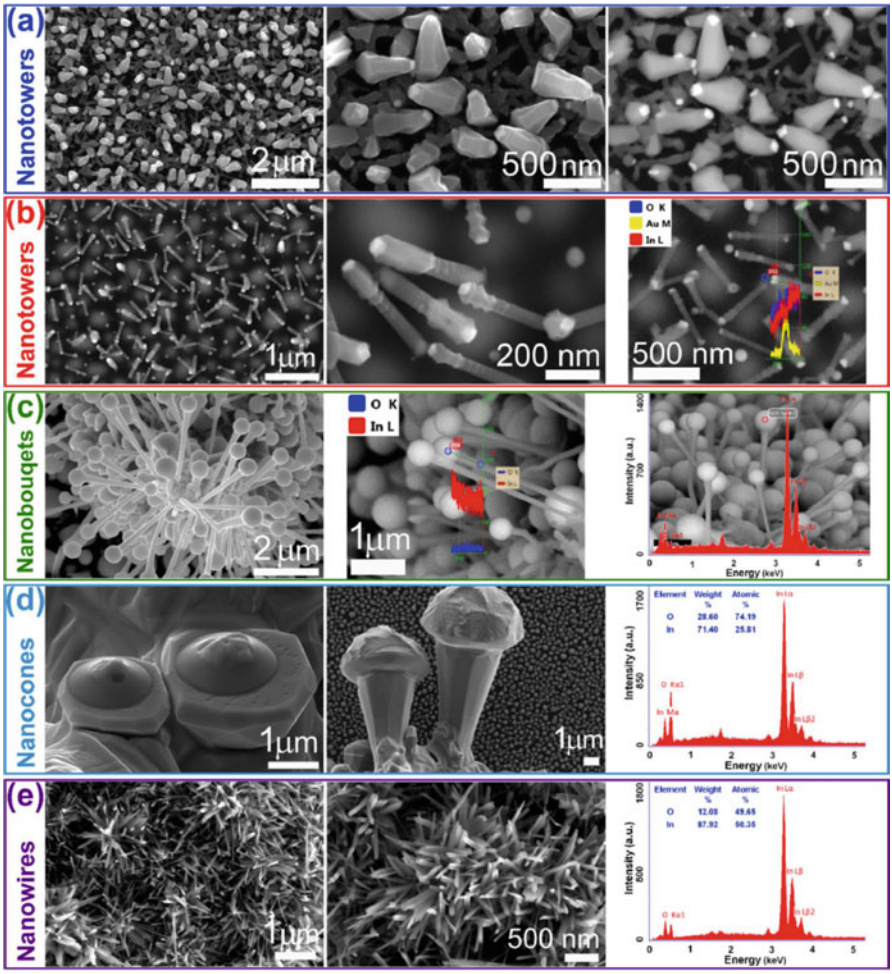

Fig. 6.26 (**a**) Low- and high-magnification FESEM images of In_2O_3 nanotowers grown in sample A and their backscattered electron image; (**b**) low- and high-magnification FESEM images of In_2O_3 nanotowers grown in sample B and their line scanning EDS analysis; (**c**) FESEM images of In_2O_3 nanobouquets grown in sample C and their line scanning and point EDS analyses; (**d**) FESEM images of In_2O_3 nanocones with complete and incomplete growth in sample D and their EDS analysis; (**e**) low- and high-magnification FESEM images of In_2O_3 nanowires grown in sample E and their EDS analysis (With permission of Tuzluca et al. 2018)

As noted, nanostructured and three-dimensional nanorod of In_2O_3 deposited on stainless steel (SS) by a novel potentiodynamic method at a high scan rate of 200 mV s^{-1} exhibited high specific capacitance, high power density and long-term stability when used as active electrode materials for redox supercapacitors

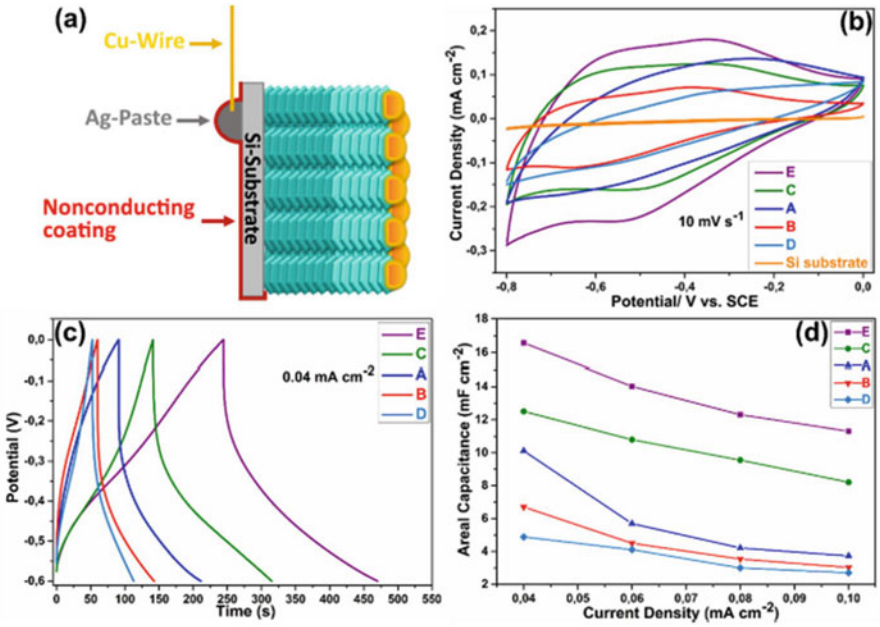

Fig. 6.27 (**a**) The schematic indicating the fabrication process of samples for electrochemical analyses; (**b**) Si substrate material and CV curves of all samples obtained at 10 mV s^{-1}; (**c**) GCD curves of all samples at 0.04 mA cm^{-2}; (**d**) Areal capacitance values of all samples at the current densities of 0.04, 0.06, 0.08, and 0.1 mA cm^{-2} (With permission of Tuzluca et al. 2018)

(Kalakodimi Rajendra Prasad et al. 2004). In_2O_3 nanowires exhibited better electrochemical performance. It is also worth stating that an increase in the surface area of an electrode leads to decrease in the ionic diffusion paths; thus, electrode materials with nanowire morphology can increase the electrochemical performance of supercapacitors.

Carbon-based materials were also used to improve on the electrochemical performance of In_2O_3-based electrodes and have shown great improvements. Fine In_2O_3 nanoparticles were successfully synthesized within the mesopores by thermal decomposition of a metal source. The obtained metal oxide-impregnated mesoporous carbon was effectively utilized for the enhancement of capacitive performance through a combination of both faradaic and non-faradaic processes, and the composite exhibited a high capacitance of 275 F g^{-1} in 1 M Na_2SO_4 (Bastakoti et al. 2013), demonstrating an addition of carbon materials as a strategy to improving energy density of supercapacitors. Table 6.1 summarizes the electrochemical performances of some transition metal oxide-based materials for application in supercapacitors (SCs) obtained from the literature.

Table 6.1 Summary of electrochemical performances of some transition metal oxide-based materials for application in supercapacitors (SCs)

Electrode material	Cell voltage (V)	Cell configuration	Aqueous electrolyte	Specific capacitance	Specific current/scan rate	Energy density (Wh kg^{-1})	Power density (kW kg^{-1})	Capacitance retention	References
RuO_2	1.6	2-electrode, symmetric	1 M Na_2SO_4	53.0 F g^{-1}	0.625 A g^{-1}	18.8	10.0	92% (2000 cycles)	Xia et al. (2012)
RuO_2//MXene	1.5	2-electrode, asymmetric	1 M H_2SO_4	93.0 F g^{-1}	50 mV s^{-1}	29.0	26.0	86% (20 000)	Jiang et al. (2018)
LSG/RuO_2// AC	1.8	2-electrode, asymmetric	1 M Na_2SO_4	8.6 F cm^{-3}	0.5 Acm^{-3}	55.3	81.4	–	Hwang et al. (2015)
RuO_2-Gr	1.5	2-electrode, symmetric	2 M Li_2SO_4	140 F g^{-1}	1.0 A g^{-1}	43.8	37.5	93% (10,000 cycles)	Li and He (2018)
OLC/MnO_2	0.8	2-electrode, symmetric	1 M Na_2SO_4	254 F g^{-1}	0.1 A g^{-1}	5.6	74.8	–	Makgopa et al. (2015)
$MnO_{2(SDS)}$/ GO//GO	1.8	2-electrode, asymmetric	1 M Li_2SO_4	280 F g^{-1}	0.5 A g^{-1}	35.0	7.2	70% (1000 cycles)	Jafta et al. (2013)
GF/MnO_2	1.0	2-electrode, symmetric	1 M Na_2SO_4	240 F g^{-1}	0.1 A g^{-1}	34	20	100% (1000 cycles).	Bello et al. (2013b)
SnO_2/MnO_2	1.0	2-electrode, symmetric	1 M Na_2SO_4	800 F g^{-1}	1 A g^{-1}	35.4	25	99% (2000 cycles)	Yan et al. (2010)
rGO/Mn_2O_3/ Mn_3O_4//rGO	1.4	2-electrode, asymmetric	1 M Na_2SO_4	133 F g^{-1}	0.2 A g^{-1}	9.1	26.4	83% (1000 cycles)	Chidembo et al. (2014)
MnO_2-NW/Gr// Gr	2.0	2-electrode, asymmetric	1 M Na_2SO_4	32.0 F g^{-1}	0.5 A g^{-1}	30.4	5.0	79% (1000 cycles)	Wu et al. (2010)
MnO_2/OLC	0.8	3-electrode	1 M Na_2SO_4	177.5 F g^{-1}	2 A g^{-1}	–	–	101% (1000 cycles)	Wang et al. (2012c)
NW-MnO_2	0.8	3-electrode	Gel electrolyte (3 wt.% SiO_2)	151 F g^{-1}	100 mV s^{-1}	–	–	–	Nam et al. (2010)
MnO_2	1.0	3-electrode	1 M LiOH	317 F g^{-1}	0.1 A g^{-1}	–	–	80% (2000 cycles)	Wang et al. (2007)

$MnO_2.nH_2O$	1.2	3-electrode	2 M KCl	200 F g^{-1}	2 mA/cm^2	–	–	100% (100 cycles)	Lee and Goodenough (1999)
MnO_2/NF-Gr	1.0	3-electrode	1 M Na_2SO_4	305 F g^{-1}	1 A g^{-1}	–	–	80% (1000 cycles)	Bello et al. (2013a)
Birnessite-type MnO_2	0.8	3-electrode	1 M Na_2SO_4	210 F g^{-1}	0.2 A g^{-1}	–	–	98% (300 cycles)	Ming et al. (2012)
α-MnO_2	1.0	3-electrode	1 M Na_2SO_4	146 F g^{-1}	16.0 A g^{-1}	–	–	91% (400 cycles	Meher and Rao (2012)
Mn_3O_4/CNTs	1.0	3-electrode	1 M Na_2SO_4	498 F g^{-1}	5.0 mV s^{-1}	–	–	90% (2000 cycles)	Dubal and Holze (2013)
Porous Mn_3O_4	1.0	3-electrode	1 M Na_2SO_4	233 F g^{-1}	0.5 A g^{-1}	–	–	78% (5000 cycles)	Yang et al. (2015)
Mn_3O_4/MC	1.0	3-electrode	6 M KOH	266 F g^{-1}	1.0 mV s^{-1}	–	–	74% (1000 cycles)	Zhou et al. (2011)
Gr/Mn_3O_4	1.0	3-electrode	1 M Na_2SO_4	121 F g^{-1}	0.5 A g^{-1}	–	–	100% (10,000 cycles)	Lee et al. (2012)
Mn_3O_4/Gr	0.9	3-electrode	2 M KOH	237 F g^{-1}	1.0 A g^{-1}	12.0	5.4	93.68% (1000 cycles)	Wang et al. (2012)
Mn_2O_3	0.8	3-electrode	0.5 M Na_2SO_4	191 F g^{-1}	0.1 A g^{-1}	–	–	108% (3000 cycles)	Li et al. (2015)
Mn_3O_4/OLC	2.0	2-electrode, asymmetric	1 M Na_2SO_4	–	–	19.0	45.0	–	Makgopa et al. (2017)
NiO//Fe_2O_3/CFP	1.35	2-electrode, asymmetric	2 M KOH	908 F g^{-1}	2 A g^{-1}	105	12.7	–	Tang et al. (2015)
Fe_3O_4	0.7	3-electrode	1 M Na_2SO_3	170 F g^{-1}	2.0 mV s^{-1}	–	–	–	Wang et al. (2006)
Fe_3O_4/Carbon	1.0	3-electrode	1 M KOH	139 F g^{-1}	0.5 A g^{-1}	–	–	83.3% (4000 cycles)	Meng et al. (2014)
	1.0	3-electrode	1 M Na_2SO_3	165 F g^{-1}	0.2 A g^{-1}	–	–		

(continued)

Table 6.1 (continued)

Electrode material	Cell voltage (V)	Cell configuration	Aqueous electrolyte	Specific capacitance	Specific current/scan rate	Energy density (Wh kg^{-1})	Power density (kW kg^{-1})	Capacitance retention	References
Fe_3O_4/MWCNT								85.1% (1000 cycles)	Kim and Park (2011)
SiCF/Fe_3O_4	1.2	3-electrode	1 M KOH	423 F g^{-1}	5 mV s^{-1}	–	–	90.3% (5000 cycles)	Kim and Kim (2017)
GF/CNT@Fe_2O_3//GF/$CoMoO_4$	1.6	2-electrode, asymmetric	2 M KOH	210 F g^{-1}	–	74.7	11.2	95.4% (50,000 cycles)	Guan et al. (2015)
V_2O_5/TiO_2-NT	0.8	3-electrode	0.1 M $HClO_4$	220 F g^{-1}	0.2 mA/cm^2	19.56	–	–	Yang et al. (2011b)
V_2O_5-NW	1.2	3-electrode	1 M $LiNO_3$	351 F g^{-1}	2 A g^{-1}	–	–	–	Wang et al. (2015)
V_2O_5/PPY	1.0	3-electrode	5 M $LiNO_3$	559 F g^{-1}	3 A g^{-1}	–	–	70% (100 cycles.)	Yang et al. (2013)
3D V_2O_5	2.0	2-electrode, symmetric	1 M Na_2SO_4	451 F g^{-1}	0.5 A g^{-1}	107	9.4	90% (4000 cycles)	Zhu et al. (2013)
V_2O_5	0.9	2-electrode, symmetric	2 M KCl	190 F g^{-1}	0.1 A g^{-1}	578	−1.8	–	Wee et al. (2010)
	3.0		1 M $LiClO_4$ in PC	250 F g^{-1}					
V_2O_5/PANI	2.0	2-electrode, symmetric	5 M LiCl	412 F g^{-1}	4.5 mA/cm^2	82	0.8	80% (5000 cycles)	Bai et al. (2014)
VO/VO_x/CNF	1.0	2-electrode, symmetric	6 M KOH	326 F g^{-1}	1 A g^{-1}	10	0.96	92% (5000 cycles)	Tang et al. (2016)
2D VO_2-NS	1.4	2-electrode, symmetric	1 M $LiClO_4$ in PC	405 F g^{-1}	1 A g^{-1}	46	1.4	95% (6000 cycles)	Rakhi et al. (2016)
Gr/VO_2//Gr	1.7	2-electrode, asymmetric	0.5 M K_2SO_4	225 F g^{-1}	–	22.8	8.5	81% (1000 cycles)	Deng et al. (2013)

SnO_2/rGO	1.0	3-electrode,	1 M H_2SO_4	348 F g^{-1}	0.5 A g^{-1}	32.2	1.0	–	Hsieh et al. (2014)
SnO_2/Ti_3C_2	0.7	3-electrode	6 M KOH	126 F g^{-1}	1 A g^{-1}	–	–	82% (8000 cycles)	Zheng et al. (2017)

Key: *Gr* graphene, *NF* nickel foam, *GF* graphene foam, *CNT* carbon nanotube, *MWCNT* multi-walled carbon nanotube, *OLCs* onion-like carbons, *PDDA* polydiallyldimethylammonium, *rG* reduced graphene, *MC* mesoporous carbon, *CFP* carbon fibre paper, *CNF* carbon nanofibre

6.2 Summary and Future Prospects

It is evident that significant progress has been made in SC applications, which has generated worldwide attention in these energy storage/conversion devices due to the need to resolve high demands for clean and sustainable energy followed by the fact that fossil fuels have shown potential threat to the environment and thereby deemed unreliable. The advantages of SC systems account to their high power density, high efficiency and long-life expectancy. However, the development of these energy storage devices depends upon the innovative ways of fine-tuning their electrode materials. Metal oxide nanostructured materials with their interesting properties such as low cost, good electrochemical response, various oxidation states and availability have proven themselves as attractive electrode materials for energy storage applications since they can be easily synthesized from various synthetic routes even though their synthesis and application are still restricted to the lab-scale production. Much of the limitation of the use of metal-oxides in SCs could be attributed to the low conductivity and agglomeration upon rapid cycling, which limits their electrochemical performance to match their theoretical estimation, thus hindering their commercial applications. Intensive work has been devoted in mitigating the above limitation by incorporation of highly conductive materials such as carbon allotropes and recently MXENES to make composite materials with an improved electrochemical performance and stability upon long-time cycling. The approach of discovering new materials that boosts the properties of metal oxides has drastically improved the rapid use of these nanostructured materials as EC electrode materials. Therefore, the innovation that further improves the existing metal oxide electrodes while also promoting their novel composites that results in stable fabrication in order to meet the market demand of EC technology is of great importance. From the literature and data presented in this work, it is very clear that the performance of metal-based oxides for supercapacitor applications has increased exponentially over the last decade and continues to improve. Specific capacitance, energy and power density values continue to improve, while the storage mechanisms of most of the oxide-based supercapacitors continue to be widely studied and understood. Efforts to produce SCs from renewable materials also encourage optimism that such an environmentally friendly option may soon be feasible for use on a larger scale. Currently, supercapacitors are being used for some small applications, and with the rapid improvement of their energy densities, it is only a matter of time before their industrial applications become common. The future of supercapacitor research is endlessly promising; however, there are certain things that should be taken into account in order to ensure that all future research can be used fully. One of the challenges is that results are communicated in multiple different ways, and this can make it difficult to compare different studies. Most studies choose to express their results in terms of specific capacitance, $F \cdot g^{-1}$, measured at different scan rates, $mV \cdot s^{-1}$ and/ or specific current, $A \cdot g^{-1}$. Some papers, however, choose to express

specific current in $mA \cdot cm^{-2}$, and specific capacitance in $mF \cdot cm^{-2}$, making it difficult to compare the performance of the subject material to that of others in the literature when additional information, such as the density of the material, is not provided. However, F/cm^2 is justified while the mass of electrode materials is beyond the measurable limit and as well for micro-supercapacitor. Therefore, it is recommended that for future studies, a standard be developed for such aspects of the research so that all materials may be accurately compared. The recent upsurge in the quantity of research carried out on the various oxide-based supercapacitors, as well as the quality of SCs being produced, has well-established their position in the field of energy storage. In order to fully succeed on the generation of the reliable, efficient and effective technology that can mitigate the global energy demand, more conductive materials obtained from different sources and various synthetic routes should be explored and be incorporated on these metal oxides. Another major drawback in the development of supercapacitor technology is the relatively high cost associated with it when compared to other energy devices. Thus, future research should be invested towards the development of fascinating transition metal oxide nanomaterials exhibiting a high charge capacity while demonstrating a minimum electronic and electrolytic resistance in a very cost-effective manner. As research advances, and improvements continue to be made, it is certain that the future held for supercapacitors is an auspicious one.

Appendix

Potentiostat – A potentiostat is the electronic hardware required to control electrochemical cell and run most electroanalytical experiments.

Cell potential – The overall electrical potential of an electrochemical cell. It is the sum of the reduction potential of the cathode and the oxidation potential of the anode.

Electrolytic cell – A cell that consumes electrical energy to drive a non-spontaneous redox reaction.

Charge (Q) – The quantity of unbalanced electricity in a body such as an electron or an ion.

Charge density (q) – The measure of charge Q and electrode area A, i.e. $q = Q/A$.

Chronoamperometry – The techniques and methodology of studying current as a function of time.

Current (I) – The rate of charge flow or passage, i.e. $I = (dQ/dt)$.

Specific current – The measure of current I and electrode mass g, i.e. $i = I/g$.

Cyclic voltammogram (CV) – A plot of current on the y-axis against potential on the x-axis during a voltammetric experiment in which the potential is ramped twice, once forward to the switch potential and then back again.

Electrochemical area – The area of an electrode; the area that an electrode is 'perceived' to have.

Electrochemical cell – An electrochemical cell typically consists of two electronic conductors (also called electrodes) – An ionic conductor (called an electrolyte).

Electrode – A conductor employed either to determine an electrode potential (at zero current, i.e. for potentiometric experiments) or to determine current during a dynamic electroanalytical measurement. The electronic conductivity of most electrodes is metallic.

A reaction is classified as oxidation or reduction depending on the direction of electron transfer. There are two fundamental types of half-cell reactions: – Oxidation reactions – Reduction reactions

Oxidation – Involves the loss of an electron and involves the transfer of electrons from the species to the electrode $R = O + ne$

Reduction – Involves the gain of an electron and involves the transfer of electrons from the electrode to the species $O + ne = R$.

Electrode at which the oxidation reaction occurs is called the anode.

Electrode at which the reduction reaction occurs is called the cathode.

Anodic current – An anodic current is the flow of electrical charge (usually carried by electrons) into a working electrode from a second phase (usually an electrolyte solution) as a result of the oxidation of one or more species in the second phase.

Cathodic current – A cathodic current is the flow of electrical charge (usually carried by electrons) out of a working electrode into a second phase (usually an electrolyte solution) leading to the reduction of one or more species in the second phase.

The electrode at which the reaction of interest occurs is called the working electrode.

The electrode at which the other (coupled) reaction occurs is called the counter electrode.

A third electrode, called the reference electrode, may also be used. An ideal reference electrode is one that maintains a constant potential irrespective of the amount of current (if any) that is passed through it.

Electrode potential – The electrode potential for a reaction is derived directly from the free energy change for that reaction $\Delta G = -NFE$. The standard oxidation potential is equal in magnitude but opposite in sign to the std. reduction potential.

Electrolyte – An ionic salt to be dissolved in a solvent or the solution formed by dissolving an ionic salt in a solvent.

Electrolytic processes – Reactions in which chemical changes occur on the passage of an electrical current.

Galvanic or voltaic processes – Chemical reactions that result in the production of electrical energy.

References

An G, Yu P, Xiao M et al (2008) Low-temperature synthesis of Mn_3O_4 nanoparticles loaded on multi-walled carbon nanotubes and their application in electrochemical capacitors. Nanotechnology 19:275709. https://doi.org/10.1088/0957-4484/19/27/275709

Arlinghaus FJ (1974) Energy bands in stannic oxide (SnO_2). J Phys Chem Solids 35:931–935. https://doi.org/10.1016/S0022-3697(74)80102-2

Augustyn V, Come J, Lowe MA et al (2013) High-rate electrochemical energy storage through Li^+ intercalation pseudocapacitance. Nat Mater 12:518–522. https://doi.org/10.1038/nmat3601

Augustyn V, Simon P, Dunn B (2014) Pseudocapacitive oxide materials for high-rate electrochemical energy storage. Energy Environ Sci 7:1597. https://doi.org/10.1039/c3ee44164d

Bai MH, Bian LJ, Song Y, Liu XX (2014) Electrochemical codeposition of vanadium oxide and polypyrrole for high-performance supercapacitor with high working voltage. ACS Appl Mater Interfaces 6:12656–12664. https://doi.org/10.1021/am502630g

Bang H, Ellinger AE, Hadjimarcou J, Traichal PA (2000) Consumer concern, knowledge, belief, and attitude toward renewable energy: an application of the reasoned action theory. Psychol Mark 17:449–468

Bastakoti BP, Oveisi H, Hu C-C et al (2013) Mesoporous carbon incorporated with In_2O_3 nanoparticles as high-performance supercapacitors. Eur J Inorg Chem 2013:1109–1112. https://doi.org/10.1002/ejic.201201311

Baykal A, Kavas H, Durmuş Z et al (2010) Sonochemical synthesis and chracterization of Mn_3O_4 nanoparticles. Cent Eur J Chem 8:633–638. https://doi.org/10.2478/s11532-010-0037-8

Béguin F, Raymundo-Piñero E, Frackowiak E (2009) Electrical double-layer capacitors and pseudocapacitors. CRC Press, Boca Raton

Béguin F, Presser V, Balducci A, Frackowiak E (2014) Carbons and electrolytes for advanced supercapacitors. Adv Mater 26:2219–2251., 2283. https://doi.org/10.1002/adma.201304137

Bello A, Fashedemi OO, Fabiane M et al (2013a) Microwave assisted synthesis of MnO_2 on nickel foam-graphene for electrochemical capacitor. Electrochim Acta 114:48. https://doi.org/10.1016/j.electacta.2013.09.134

Bello A, Fashedemi OO, Lekitima JN et al (2013b) High-performance symmetric electrochemical capacitor based on graphene foam and nanostructured manganese oxide. AIP Adv 3:82118

Bonu V, Gupta B, Chandra S et al (2016) Electrochemical supercapacitor performance of SnO_2 quantum dots. Electrochim Acta 203:230–237. https://doi.org/10.1016/J.ELECTACTA.2016.03.153

Borgohain R, Selegue JP, Cheng Y-T (2014) Ternary composites of delaminated-MnO_2 /PDDA/functionalized-CNOs for high-capacity supercapacitor electrodes. J Mater Chem A 2:20367–20373. https://doi.org/10.1039/C4TA04439H

Brousse T, Toupin M, Dugas R et al (2006) Crystalline MnO_2 as possible alternatives to amorphous compounds in electrochemical supercapacitors. J Electrochem Soc 153:A2171. https://doi.org/10.1149/1.2352197

Burda C, Chen X, Narayanan R, El-Sayed MA (2005) Chemistry and properties of nanocrystals of different shapes. Chem Rev 105:1025–1102

Burke A (2000) Ultracapacitors: why, how, and where is the technology. J Power Sources 91:37–50. https://doi.org/10.1016/S0378-7753(00)00485-7

Burke A, Liu Z, Zhao H (2014, December) Present and future applications of supercapacitors in electric and hybrid vehicles. https://doi.org/10.1109/IEVC.2014.7056094 Conference: IEEE International Electric Vehicle Conference 2014, Florence 17–19

Bykova E, Dubrovinsky L, Dubrovinskaia N et al (2016) Structural complexity of simple Fe_2O_3 at high pressures and temperatures. Nat Commun 7:10661. https://doi.org/10.1038/ncomms10661

Cao L, Zhu J, Li Y et al (2014) Ultrathin single-crystalline vanadium pentoxide nanoribbon constructed 3D networks for superior energy storage. J Mater Chem A 2:13136–13142. https://doi.org/10.1039/C4TA02229G

Chang J, Lee W, Mane RS et al (2008) Morphology-dependent electrochemical supercapacitor properties of indium oxide. Electrochem Solid-State Lett 11:A9. https://doi.org/10.1149/1.2805996

Chen Z, Zhang S, TAn S et al (1997) Preparation and electron spin resonance effect of nanometer-sized Mn_2O_3. J Cryst Growth 180:280–283. https://doi.org/10.1016/S0022-0248(97)00215-7

Chen X, Li X, Jiang Y et al (2005) Rational synthesis of MnO_2 and Mn_2O_3 nanowires with the electrochemical characterization of MnO_2 nanowires for supercapacitor. Solid State Commun 136:94–96. https://doi.org/10.1016/j.ssc.2005.06.033

Chen Z, Qin Y, Weng D et al (2009) Design and synthesis of hierarchical nanowire composites for electrochemical energy storage. Adv Funct Mater 19:3420–3426. https://doi.org/10.1002/adfm.200900971

Chen JS, Archer LA, Wen (David) Lou X (2011a) SnO_2 hollow structures and TiO_2 nanosheets for lithium-ion batteries. J Mater Chem 21:9912. https://doi.org/10.1039/c0jm04163g

Chen Z, Augustyn V, Wen J et al (2011b) High-performance supercapacitors based on intertwined CNT/V_2O_5 nanowire nanocomposites. Adv Mater 23:791–795. https://doi.org/10.1002/adma.201003658

Cheng H-W, Zhou C, Mai L et al (2008) Field emission from $V_2O_5nH_2O$ Nanorod arrays. J Phys Chem C 112:2262–2265. https://doi.org/10.1021/JP0766151

Chiang NK, Clokec M, Chena GZ et al (2006) Nano-sized Mn_2O_3 preparedby a novel solvolysis route as an electrochemical capacitor. Inst Eng Malaysia 69:31–36

Chidembo AT, Aboutalebi SH, Konstantinov K et al (2014) In situ engineering of urchin-like reduced graphene oxide–Mn_2O_3–Mn_3O_4 nanostructures for supercapacitors. RSC Adv 4:886–892. https://doi.org/10.1039/c3ra44973d

Choi D, Blomgren GE, Kumta PN (2006) Fast and reversible surface redox reaction in nanocrystalline vanadium nitride supercapacitors. Adv Mater 18:1178–1182

Conway BE (1999) Electrochemical supercapacitors: scientific fundamentals and technological applications. Kluwer Academic/Plenum, New York

Cottineau T, Toupin M, Delahaye T et al (2006) Nanostructured transition metal oxides for aqueous hybrid electrochemical supercapacitors. Appl Phys A Mater Sci Process 82:599–606

Deb SK (2008) Opportunities and challenges in science and technology of WO_3 for electrochromic and related applications. Sol Energy Mater Sol Cells 92:245–258. https://doi.org/10.1016/J.SOLMAT.2007.01.026

Deng L, Zhang G, Kang L et al (2013) Graphene/VO_2 hybrid material for high performance electrochemical capacitor. Electrochim Acta 112:448–457. https://doi.org/10.1016/J.ELECTACTA.2013.08.158

Djurfors B, Broughton JN, Brett MJ, Ivey DG (2005) Electrochemical oxidation of Mn/MnO films: formation of an electrochemical capacitor. Acta Mater 53:957–965. https://doi.org/10.1016/j.actamat.2004.10.041

Dong R, Ye Q, Kuang L et al (2013) Enhanced supercapacitor performance of Mn_3O_4 nanocrystals by doping transition-metal ions. ACS Appl Mater Interfaces 5:9508–9516

Drache M, Roussel P, Wignacourt J-P (2007) Structures and oxide mobility in Bi−Ln−O materials: heritage of Bi_2O_3. Chem Rev 107:80–96. https://doi.org/10.1021/CR050977S

Du Y, Yan J, Meng Q et al (2012) Fabrication and excellent conductive performance of antimony-doped tin oxide-coated diatomite with porous structure. Mater Chem Phys 133:907–912. https://doi.org/10.1016/J.MATCHEMPHYS.2012.01.115

Dubal DP, Holze R (2013) A successive ionic layer adsorption and reaction (SILAR) method to induce Mn_3O_4 nanospots on CNTs for supercapacitors. New J Chem 37:403–408. https://doi.org/10.1039/c2nj40862g

Dubal DP, Dhawale DS, Salunkhe RR et al (2009) A novel chemical synthesis of interlocked cubes of hausmannite Mn_3O_4 thin films for supercapacitor application. J Alloys Compd 484:218–221. https://doi.org/10.1016/j.jallcom.2009.03.135

Dubal DP, Dhawale DS, Salunkhe RR et al (2010) Chemical synthesis and characterization of Mn_3O_4 thin films for supercapacitor application. J Alloys Compd 497:166–170. https://doi.org/10.1016/j.jallcom.2010.02.182

Fan D, Yang P (1999) Introduction to and classification of manganese deposits of China. Ore Geol Rev 15:1–13

Gao W, Ye S, Shao M (2011) Solution-combusting preparation of mono-dispersed Mn_3O_4 nanoparticles for electrochemical applications. J Phys Chem Solids 72:1027–1031. https://doi.org/10.1016/j.jpcs.2011.05.015

Ghosh A, Lee YH (2012) Carbon-based electrochemical capacitors. ChemSusChem 5:480–499. https://doi.org/10.1002/cssc.201100645

Ghosh S, Gupta B, Ganesan K et al (2016) MnO_2-vertical graphene nanosheets composite electrodes for energy storage devices. Mater Today Proc 3:1686–1692. https://doi.org/10.1016/J.MATPR.2016.04.060

Ghosh S, Jeong SM, Polaki SR (2018) A review on metal nitrides/oxynitrides as an emerging supercapacitor electrode beyond oxide. Korean J Chem Eng 35:1389–1408. https://doi.org/10.1007/s11814-018-0089-6

Greenwood N (1997) Chemistry of the elements, 2nd edn. Heinemann, Butterworth

Guan C, Liu J, Wang Y et al (2015) Iron oxide-decorated carbon for supercapacitor anodes with ultrahigh energy density and outstanding cycling stability. ACS Nano 9:5198–5207. https://doi.org/10.1021/acsnano.5b00582

Gujar TP, Shinde VR, Lokhande CD, Han S-H (2006) Electrosynthesis of Bi_2O_3 thin films and their use in electrochemical supercapacitors. J Power Sources 161:1479–1485. https://doi.org/10.1016/J.JPOWSOUR.2006.05.036

Gustafson KPJ, Shatskiy A, Verho O et al (2017) Water oxidation mediated by ruthenium oxide nanoparticles supported on siliceous mesocellular foam. Cat Sci Technol 7:293–299. https://doi.org/10.1039/C6CY02121B

Hatzell KB, Fan L, Beidaghi M et al (2014) Composite manganese oxide percolating networks as a suspension electrode for an asymmetric flow capacitor. ACS Appl Mater Interfaces 6:8886–8893. https://doi.org/10.1021/am501650q

Hatzell KB, Boota M, Kumbur EC, Gogotsi Y (2015) Flowable conducting particle networks in redox-active electrolytes for grid energy storage. J Electrochem Soc 162:A5007–A5012. https://doi.org/10.1149/2.0011505jes

He W, Zhang Y, Zhang X et al (2003) Low temperature preparation of nanocrystalline Mn_2O_3 via ethanol-thermal reduction of MnO_2. J Cryst Growth 252:285–288. https://doi.org/10.1016/S0022-0248(03)00937-0

Hou X, Liu B, Wang X et al (2013) SnO_2-microtube-assembled cloth for fully flexible self-powered photodetector nanosystems. Nanoscale 5:7831. https://doi.org/10.1039/c3nr02300a

Hsieh C-T, Lee W-Y, Lee C-E, Teng H (2014) Electrochemical capacitors fabricated with tin oxide/graphene oxide nanocomposites. J Phys Chem C 118:15146–15153. https://doi.org/10.1021/jp502958w

Hu C, Tsou T (2002) Ideal capacitive behavior of hydrous manganese oxide prepared by anodic deposition. Electrochem Commun 4:105–109

Hu C-C, Chang K-H, Lin M-C, Wu Y-T (2006) Design and tailoring of the nanotubular arrayed architecture of hydrous RuO_2 for next generation supercapacitors. Nano Lett 6:2690–2695

Huang Z, Chai C, Tan X et al (2007) Photoluminescence properties of the In_2O_3 octahedrons synthesized by carbothermal reduction method. Mater Lett 61:5137–5140. https://doi.org/10.1016/J.MATLET.2007.04.062

Hui-Chi Chiu C-SY (2007) Hydrothermal synthesis of SnO_2 nanoparticles and their gas-sensing of alcohol. J Phys Chem C 111:7256–7259. https://doi.org/10.1021/JP0688355

Hwang JY, El-Kady MF, Wang Y et al (2015) Direct preparation and processing of graphene/RuO_2 nanocomposite electrodes for high-performance capacitive energy storage. Nano Energy 18:57–70. https://doi.org/10.1016/j.nanoen.2015.09.009

IEA (2014) With projections to 2040. In: Int. Energy Outlook 2014

Jafta CJ, Nkosi F, le Roux L et al (2013) Manganese oxide/graphene oxide composites for high-energy aqueous asymmetric electrochemical capacitors. Electrochim Acta 110:228–233. https://doi.org/10.1016/j.electacta.2013.06.096

Jiang J, Kucernak A (2002) Electrochemical supercapacitor material based on manganese oxide: preparation and characterization. Electrochim Acta 47:2381–2386. https://doi.org/10.1016/S0013-4686(02)00031-2

Jiang H, Lee PS, Li C (2013) 3D carbon based nanostructures for advanced supercapacitors. Energy Environ Sci 6:41–53

Jiang Q, Kurra N, Alhabeb M et al (2018) All pseudocapacitive MXene-RuO_2 asymmetric supercapacitors. Adv Energy Mater 1703043:1703043. https://doi.org/10.1002/aenm.201703043

Jo C, Hwang I, Lee J et al (2011) Investigation of pseudocapacitive charge-storage behavior in highly conductive ordered mesoporous tungsten oxide electrodes. J Phys Chem C 115:11880–11886. https://doi.org/10.1021/jp2036982

Johan E. ten Elshof, Yuan H, Gonzalez Rodriguez P (2016) Two-dimensional metal oxide and metal hydroxide nanosheets: synthesis, controlled assembly and applications in energy conversion and storage. Adv Energy Mater 6:1600355. https://doi.org/10.1002/aenm.201600355

Kawasaki BS, Garside BK, Shewchun J (1970) Electron beam luminescence of SnO_2. Proc IEEE 58:179–180. https://doi.org/10.1109/PROC.1970.7583

Kim M, Kim J (2017) Synergistic interaction between pseudocapacitive Fe_3O_4 nanoparticles and highly porous silicon carbide for high-performance electrodes as electrochemical supercapacitors. Nanotechnology 28:195401. https://doi.org/10.1088/1361-6528/aa6812

Kim Y-T, Mitani T (2006) Oxidation treatment of carbon nanotubes: an essential process in nanocomposite with RuO_2 for supercapacitor electrode materials. Appl Phys Lett 89:033107. https://doi.org/10.1063/1.2221872

Kim Y-H, Park S-J (2011) Roles of nanosized Fe_3O_4 on supercapacitive properties of carbon nanotubes. Curr Appl Phys 11:462–466. https://doi.org/10.1016/J.CAP.2010.08.018

Kim HW, Shim SH, Lee C (2006) SnO2 microparticles by thermal evaporation and their properties. Ceram Int 32:943–946. https://doi.org/10.1016/J.CERAMINT.2005.06.015

Korotcenkov G, Brinzari V, Cerneavschi A et al (2002) Crystallographic characterization of In2O3 films deposited by spray pyrolysis. Sensors Actuators B Chem 84:37–42. https://doi.org/10.1016/S0925-4005(02)00008-4

Lee HY, Goodenough JBJB (1999) Supercapacitor behavior with KCl electrolyte. J Solid State Chem 144:220–223. https://doi.org/10.1006/jssc.1998.8128

Lee JW, Hall AS, Kim J-D, Mallouk TE (2012) A facile and template-free hydrothermal synthesis of Mn_3O_4 Nanorods on graphene sheets for supercapacitor electrodes with long cycle stability. Chem Mater 24:1158–1164. https://doi.org/10.1021/cm203697w

Li M, He H (2018) Nickel-foam-supported ruthenium oxide/graphene sandwich composite constructed via one-step electrodeposition route for high-performance aqueous supercapacitors. Appl Surf Sci 439:612–622. https://doi.org/10.1016/j.apsusc.2018.01.064

Li Y, Yao J, Uchaker E et al (2013) Leaf-like V_2O_5 Nanosheets fabricated by a facile green approach as high energy cathode material for Lithium-ion batteries. Adv Energy Mater 3:1171–1175. https://doi.org/10.1002/aenm.201300188

Li W, Shao J, Liu Q et al (2015) Facile synthesis of porous Mn_2O_3 nanocubics for high-rate supercapacitors. Electrochim Acta 157:108–114. https://doi.org/10.1016/j.electacta.2015.01.056

Li Q, Zheng S, Xu Y et al (2018) Ruthenium based materials as electrode materials for supercapacitors. Chem Eng J 333:505–518. https://doi.org/10.1016/j.cej.2017.09.170

Liu F-A, Yang Y-C, Liu J et al (2012) Preparation of Bi_2O_3@Bi_2S_3 core–shell nanoparticle assembled thin films and their photoelectrochemical and photoresponsive properties. J Electroanal Chem 665:58–62. https://doi.org/10.1016/J.JELECHEM.2011.11.015

Liu Y, Jiao Y, Zhang Z et al (2014) Hierarchical SnO_2 nanostructures made of intermingled ultrathin nanosheets for environmental remediation, smart gas sensor, and supercapacitor applications. ACS Appl Mater Interfaces 6:2174–2184. https://doi.org/10.1021/am405301v

Liu J, Huang S, He L (2015a) Metal-catalyzed growth of In_2O_3 nanotowers using thermal evaporation and oxidation method. J Semicond 36:123007. https://doi.org/10.1088/1674-4926/36/12/123007

Liu T, Zhao Y, Gao L, Ni J (2015b) Engineering Bi_2O_3-Bi_2S_3 heterostructure for superior lithium storage. Sci Rep 5:9307. https://doi.org/10.1038/srep09307

Liu Y, Wei J, Tian Y, Yan S (2015c) The structure–property relationship of manganese oxides: highly efficient removal of methyl orange from aqueous solution. J Mater Chem A 3:19000–19010. https://doi.org/10.1039/C5TA05507E

Luo J, Liu J, Zeng Z et al (2013) Three-dimensional graphene foam supported Fe_3O_4 lithium battery anodes with long cycle life and high rate capability. Nano Lett 13:6136–6143. https://doi.org/10.1021/nl403461n

Ma S-B, Nam K-W, Yoon W-S et al (2008) Electrochemical properties of manganese oxide coated onto carbon nanotubes for energy-storage applications. J Power Sources 178:483–489. https://doi.org/10.1016/j.jpowsour.2007.12.027

Makgopa K, Ejikeme PM, Jafta CJ et al (2015) A high-rate aqueous symmetric pseudocapacitor based on highly graphitized onion-like carbon/birnessite-type manganese oxide nanohybrids. J Mater Chem A 3:3480–3490

Makgopa K, Ejikeme PM, Ozoemena KI (2016) Nanostructured manganese oxides in supercapacitors. In: KOzoemena KI, Chen S (eds) Nanomaterials in advanced batteries and supercapacitors. Springer, New York, pp 345–376

Makgopa K, Raju K, Ejikeme PM, Ozoemena KI (2017) High-performance Mn_3O_4/onion-like carbon (OLC) nanohybrid pseudocapacitor: unravelling the intrinsic properties of OLC against other carbon supports. Carbon 117:20–32. https://doi.org/10.1016/j.carbon.2017.02.050

Manikandan K, Dhanuskodi S, Maheswari N, Muralidharan G (2016) SnO_2 nanoparticles for supercapacitor application. In: AIP conference proceedings. AIP Publishing LLC, p 050048

Meher SK, Rao GR (2012) Enhanced activity of microwave synthesized hierarchical MnO_2 for high performance supercapacitor applications. J Power Sources 215:317–328. https://doi.org/10.1016/J.JPOWSOUR.2012.04.104

Meng W, Chen W, Zhao L et al (2014) Porous Fe_3O_4/carbon composite electrode material prepared from metal-organic framework template and effect of temperature on its capacitance. Nano Energy 8:133–140. https://doi.org/10.1016/J.NANOEN.2014.06.007

Miller JM (1997) Deposition of ruthenium nanoparticles on carbon aerogels for high energy density supercapacitor electrodes. J Electrochem Soc 144:L309. https://doi.org/10.1149/1.1838142

Miller JRJ, Burke AFA (2008) Electrochemical capacitors: challenges and opportunities for real-world applications. Electrochem Soc Interface 17:53

Min J, Kierzek K, Chen X et al (2017) Facile synthesis of porous iron oxide/graphene hybrid nanocomposites and potential application in electrochemical energy storage. New J Chem 41:13553–13559. https://doi.org/10.1039/C7NJ03416D

Ming B, Li J, Kang F et al (2012) Microwave–hydrothermal synthesis of birnessite-type MnO_2 nanospheres as supercapacitor electrode materials. J Power Sources 198:428–431. https://doi.org/10.1016/j.jpowsour.2011.10.003

Mitchell E, Gupta RK, Mensah-Darkwa K et al (2014) Facile synthesis and morphogenesis of superparamagnetic iron oxide nanoparticles for high-performance supercapacitor applications. New J Chem 38:4344–4350. https://doi.org/10.1039/C4NJ00741G

Nagarajan N, Humadi H, Zhitomirsky I (2006) Cathodic electrodeposition of MnO_x films for electrochemical supercapacitors. Electrochim Acta 51:3039–3045. https://doi.org/10.1016/j.electacta.2005.08.042

Nam HS, Kwon JS, Kim KM et al (2010) Supercapacitive properties of a nanowire-structured MnO_2 electrode in the gel electrolyte containing silica. Electrochim Acta 55:7443–7446. https://doi.org/10.1016/j.electacta.2010.02.027

Nathan T, Cloke M, Prabaharan SRS (2008) Electrode properties of Mn2O3 nanospheres synthesized by combined sonochemical/solvothermal method for use in electrochemical capacitors. J Nanomater 1: https://doi.org/10.1155/2008/948183

Ng CH, Lim HN, Hayase S et al (2018) Effects of temperature on electrochemical properties of bismuth oxide/manganese oxide pseudocapacitor. Ind Eng Chem Res 57:2146–2154. https://doi.org/10.1021/acs.iecr.7b04980

Ni J, Lu W, Zhang L et al (2009) Low-temperature synthesis of monodisperse 3D manganese oxide nanoflowers and their pseudocapacitance properties. J Phys Chem 113:54–60. https://doi.org/10.1021/jp806454r

Osiak M, Khunsin W, Armstrong E et al (2013) Epitaxial growth of visible to infra-red transparent conducting In_2O_3 nanodot dispersions and reversible charge storage as a Li-ion battery anode. Nanotechnology 24:065401. https://doi.org/10.1088/0957-4484/24/6/065401

Ozkaya T, Toprak MS, Baykal A et al (2009) Synthesis of Fe_3O_4 nanoparticles at 100°C and its magnetic characterization. J Alloys Compd 472:18–23. https://doi.org/10.1016/J.JALLCOM.2008.04.101

Padmanathan N, Shao H, McNulty D et al (2016) Hierarchical NiO–In_2O_3 microflower (3D)/nanorod (1D) hetero-architecture as a supercapattery electrode with excellent cyclic stability. J Mater Chem A 4:4820–4830. https://doi.org/10.1039/C5TA10407F

Park J, Lee JW, Ye BU et al (2015) Structural evolution of chemically-driven RuO_2/ nanowires and 3-dimensional design for photo-catalytic applications. Sci Rep 5:1–10. https://doi.org/10.1038/srep11933

Pham DP, Phan BT, Hoang VD et al (2014) Control of preferred (222) crystalline orientation of sputtered indium tin oxide thin films. Thin Solid Films 570:16–19. https://doi.org/10.1016/J.TSF.2014.08.041

Poizot P, Dolhem F (2011) Clean energy new deal for a sustainable world: from non-CO_2 generating energy sources to greener electrochemical storage devices. Energy Environ Sci 4:2003. https://doi.org/10.1039/c0ee00731e

Potter R, Rossman G (1979) The tetravalent manganese oxides: identification , hydration , and structural relationships by infrared spectroscopy. Am Mineral 64:1199–1218

Prasad KR, Koga K, Miura N (2004) Electrochemical deposition of nanostructured indium oxide: high-performance electrode material for redox supercapacitors. Chem Mater 16:1845–1847. https://doi.org/10.1021/CM0497576

Pusawale SN, Deshmukh PR, Gunjakar JL, Lokhande CD (2013) SnO_2–RuO_2 composite films by chemical deposition for supercapacitor application. Mater Chem Phys 139:416–422. https://doi.org/10.1016/J.MATCHEMPHYS.2012.12.059

Qiao Y, Sun Q, Cui H et al (2015) Synthesis of micro/nano-structured Mn_3O_4 for supercapacitor electrode with excellent rate performance. RSC Adv. https://doi.org/10.1039/C4RA04783D

Qiu M, Sun P, Shen L et al (2016) WO_3 nanoflowers with excellent pseudo-capacitive performance and the capacitance contribution analysis. J Mater Chem A 4:7266–7273. https://doi.org/10.1039/C6TA00237D

Qu Q, Yang S, Feng X (2011) 2D Sandwich-like sheets of iron oxide grown on graphene as high energy anode material for supercapacitors. Adv Mater 23:5574–5580. https://doi.org/10.1002/adma.201103042

Qu Q, Zhu Y, Gao X, Wu Y (2012) Core-shell structure of polypyrrole grown on V_2O_5 nanoribbon as high performance anode material for supercapacitors. Adv Energy Mater 2:950–955. https://doi.org/10.1002/aenm.201200088

Ragupathy P, Park DH, Campet G et al (2009) Remarkable capacity retention of nanostructured manganese oxide upon cycling as an electrode material for supercapacitor. J Phys Chem C 113:6303–6309. https://doi.org/10.1021/jp811407q

Rakhi RB, Nagaraju DH, Beaujuge P, Alshareef HN (2016) Supercapacitors based on two dimensional VO_2 nanosheet electrodes in organic gel electrolyte. Electrochim Acta 220:601–608. https://doi.org/10.1016/J.ELECTACTA.2016.10.109

Sankar KV, Senthilkumar ST, Berchmans LJ et al (2012) Effect of reaction time on the synthesis and electrochemical properties of Mn_3O_4 nanoparticles by microwave assisted reflux method. Appl Surf Sci 259:624–630. https://doi.org/10.1016/j.apsusc.2012.07.087

Saravanakumar B, Purushothaman KK, Muralidharan G (2012) Interconnected V_2O_5 Nanoporous network for high-performance supercapacitors. ACS Appl Mater Interfaces 4:4484–4490. https://doi.org/10.1021/am301162p

Saravanakumar B, Purushothaman KK, Muralidharan G (2016) Fabrication of two-dimensional reduced graphene oxide supported V_2O_5 networks and their application in supercapacitors. Mater Chem Phys 170:266–275. https://doi.org/10.1016/J.MATCHEMPHYS.2015.12.051

Senthilkumar ST, Selvan RK, Ulaganathan M, Melo JS (2014) Fabrication of Bi_2O_3||AC asymmetric supercapacitor with redox additive aqueous electrolyte and its improved electrochemical performances. Electrochim Acta 115:518–524. https://doi.org/10.1016/J.ELECTACTA.2013.10.199

Sevilla M, Mokaya R (2014) Energy storage applications of activated carbons: supercapacitors and hydrogen storage. Energy Environ Sci 7:1250–1280. https://doi.org/10.1039/C3EE43525C

Sharma RK, Oh H-S, Shul Y-G, Kim H (2007) Carbon-supported, nano-structured, manganese oxide composite electrode for electrochemical supercapacitor. J Power Sources 173:1024–1028. https://doi.org/10.1016/j.jpowsour.2007.08.076

Shown I, Ganguly A, Chen L-C, Chen K-H (2015) Conducting polymer-based flexible supercapacitor. Energy Sci Eng 3:2–26. https://doi.org/10.1002/ese3.50

Spence W (1967) The uv absorption edge of tin oxide thin films. J Appl Phys 38:3767–3770. https://doi.org/10.1063/1.1710208

Subramanian V, Zhu H, Vajtai R et al (2005) Hydrothermal synthesis and pseudocapacitance properties of MnO2 nanostructures. J Phys Chem B 109:20207–20214

Subramanian V, Zhu H, Wei B (2006) Synthesis and electrochemical characterizations of amorphous manganese oxide and single walled carbon nanotube composites as supercapacitor electrode materials. Electrochem Commun 8:827–832. https://doi.org/10.1016/j.elecom.2006.02.027

Sudha V, Sangaranarayanan MV (2002) Underpotential deposition of metals: structural and thermodynamic considerations. J Phys Chem B 106:2699–2707. https://doi.org/10.1021/jp013544b

Tan Y, Meng L, Peng Q, Li Y (2011) One-dimensional single-crystalline Mn_3O_4 nanostructures with tunable length and magnetic properties of Mn3O4 nanowires. Chem Commun (Camb) 47:1172–1174. https://doi.org/10.1039/c0cc00978d

Tang Y, Wu D, Chen S et al (2013) Highly reversible and ultra-fast lithium storage in mesoporous graphene-based TiO_2/SnO_2 hybrid nanosheets. Energy Environ Sci 6:2447. https://doi.org/10.1039/c3ee40759d

Tang Q, Wang W, Wang G (2015) The perfect matching between the low-cost Fe_2O_3 nanowire anode and the NiO nanoflake cathode significantly enhances the energy density of asymmetric supercapacitors. J Mater Chem A 3:6662–6670. https://doi.org/10.1039/C5TA00328H

Tang K, Li Y, Li Y et al (2016) Self-reduced VO/VO_x/carbon nanofiber composite as binder-free electrode for supercapacitors. Electrochim Acta 209:709–718. https://doi.org/10.1016/J.ELECTACTA.2016.05.051

Thackeray MM, Wolverton C, Isaacs ED (2012) Electrical energy storage for transportation—approaching the limits of, and going beyond, lithium-ion batteries. Energy Environ Sci 5:7854. https://doi.org/10.1039/c2ee21892e

Thomas L, Floyd DB (2009) Electronics fundamentals: circuits, devices & applications, 6th edn. Prentice Hall Press, Upper Saddle River

Tien L-C, Chen Y-J (2013) Influence of growth ambient on the surface and structural properties of vanadium oxide nanorods. Appl Surf Sci 274:64–70. https://doi.org/10.1016/J.APSUSC.2013.02.092

Toupin M, Brousse T, Be D (2004) Charge storage mechanism of MnO_2 electrode used in aqueous electrochemical capacitor. Chem Mater 16:3184–3190

Tuzluca FN, Yesilbag YO, Akkus T, Ertugrul M (2017) Effects of graphite on the synthesis of 1-D single crystal In_2O_3 nanostructures at high temperature. Mater Sci Semicond Process 66:62–68. https://doi.org/10.1016/J.MSSP.2017.04.007

Tuzluca FN, Yesilbag YO, Ertugrul M (2018) Synthesis of In_2O_3 nanostructures with different morphologies as potential supercapacitor electrode materials. Appl Surf Sci 427:956–964. https://doi.org/10.1016/J.APSUSC.2017.08.127

UNEP (2013) Green economy and trade – trends, challenges and opportunities. In: United Nations Environmental Program

Upadhyay KK, Altomare M, Eugénio S et al (2017) On the supercapacitive behaviour of anodic porous WO3-based negative electrodes. Electrochim Acta 232:192–201. https://doi.org/10.1016/J.ELECTACTA.2017.02.131

Velmurugan V, Srinivasarao U, Ramachandran R et al (2016) Synthesis of tin oxide/graphene (SnO_2/G) nanocomposite and its electrochemical properties for supercapacitor applications. Mater Res Bull 84:145–151. https://doi.org/10.1016/J.MATERRESBULL.2016.07.015

Vijayabala V, Senthilkumar N, Nehru K, Karvembu R (2018) Hydrothermal synthesis and characterization of ruthenium oxide nanosheets using polymer additive for supercapacitor applications. J Mater Sci Mater Electron 29:323–330. https://doi.org/10.1007/s10854-017-7919-x

Vol'fkovich YM, Serdyuk TM, Vol YM (2002) Electrochemical capacitors. Russ J Electrochem 38:935–959

Wang X, Wang X, Huang W et al (2005) Sol-gel template synthesis of highly ordered MnO_2 nanowire arrays. J Power Sources 140:211–215. https://doi.org/10.1016/j.jpowsour.2004.07.033

Wang S-Y, Ho K-C, Kuo S-L, Wu N-L (2006) Investigation on capacitance mechanisms of Fe_3O_4 electrochemical capacitors. J Electrochem Soc 153:A75. https://doi.org/10.1149/1.2131820

Wang X, Yuan A, Wang Y (2007) Supercapacitive behaviors and their temperature dependence of sol-gel synthesized nanostructured manganese dioxide in lithium hydroxide electrolyte. J Power Sources 172:1007–1011. https://doi.org/10.1016/j.jpowsour.2007.07.066

Wang L, Yu Y, Chen PC et al (2008) Electrospinning synthesis of C/Fe_3O_4 composite nanofibers and their application for high performance lithium-ion batteries. J Power Sources 183:717–723. https://doi.org/10.1016/j.jpowsour.2008.05.079

Wang B, Park J, Wang C et al (2010) Mn_3O_4 nanoparticles embedded into graphene nanosheets: preparation, characterization, and electrochemical properties for supercapacitors. Electrochim Acta 55:6812–6817

Wang X, Liu L, Wang X et al (2011) Mn_2O_3/carbon aerogel microbead composites synthesized by in situ coating method for supercapacitors. Mater Sci Eng B Solid-State Mater Adv Technol 176:1232–1238. https://doi.org/10.1016/j.mseb.2011.07.003

Wang D, Li Y, Wang Q, Wang T (2012) Facile synthesis of porous Mn_3O_4 nanocrystal-graphene nanocomposites for electrochemical supercapacitors. Eur J Inorg Chem:628–635. https://doi.org/10.1002/ejic.201100983

Wang Y, Yu SF, Sun CY et al (2012c) MnO_2/onion-like carbon nanocomposites for pseudocapacitors. J Mater Chem 22:17584–17588. https://doi.org/10.1039/c2jm33558a

Wang HY, Xiao FX, Yu L et al (2014) Hierarchical α-MnO_2 nanowires@$Ni_{1-x}Mn_xO_y$ nanoflakes core-shell nanostructures for supercapacitors. Small 10:3181–3186. https://doi.org/10.1002/smll.201303836

Wang N, Zhang Y, Hu T et al (2015) Facile hydrothermal synthesis of ultrahigh-aspect-ratio V_2O_5 nanowires for high-performance supercapacitors. Curr Appl Phys 15:493–498. https://doi.org/10.1016/J.CAP.2015.01.026

Wang P, Liu H, Xu Y et al (2016a) Supported ultrafine ruthenium oxides with specific capacitance up to 1099 F g-1for a supercapacitor. Electrochim Acta 194:211–218. https://doi.org/10.1016/j.electacta.2016.02.089

Wang Y-C, Chen C-Y, Kuo C-W et al (2016b) Low-temperature grown indium oxide nanowire-based antireflection coatings for multi-crystalline silicon solar cells. Phys Status Solidi 213:2259–2263. https://doi.org/10.1002/pssa.201600005

Wee G, Soh HZ, Cheah YL et al (2010) Synthesis and electrochemical properties of electrospun V2O5 nanofibers as supercapacitor electrodes. J Mater Chem 20:6720. https://doi.org/10.1039/c0jm00059k

Wei W, Cui X, Chen W, Ivey DG (2011) Manganese oxide-based materials as electrochemical supercapacitor electrodes. Chem Soc Rev 40:1697–1721. https://doi.org/10.1039/c0cs00127a

Wei D, Scherer MRJ, Bower C et al (2012) A nanostructured electrochromic supercapacitor. Nano Lett 12:1857–1862. https://doi.org/10.1021/nl2042112

Wells AF (1984) Structural inorganic chemistry, 5th edn. Science Publications, Oxford

Wu Y-T, Hu C-C (2005) Aspect ratio controlled growth of MnOOH in mixtures of Mn_3O_4 and MnOOH single crystals for supercapacitors. Electrochem Solid-State Lett 8:A240–A244

Wu X, Yao S (2017) Flexible electrode materials based on WO_3 nanotube bundles for high performance energy storage devices. Nano Energy 42:143–150. https://doi.org/10.1016/J.NANOEN.2017.10.058

Wu N-L, Wang S-Y, Han C-Y et al (2003) Electrochemical capacitor of magnetite in aqueous electrolytes. J Power Sources 113:173–178. https://doi.org/10.1016/S0378-7753(02)00482-2

Wu Z-S, Ren W, Wang D et al (2010) High-energy MnO_2 nanowire/graphene and graphene asymmetric electrochemical capacitors. ACS Nano 4:5835–5842. https://doi.org/10.1021/nn101754k

Wu J, Huang H, Yu L, Hu J (2013) Controllable hydrothermal synthesis of MnO_2 nanostructures. Adv Mater Phys Chem 3:201–205

Xia H, Shirley Meng Y, Yuan G et al (2012) A symmetric RuO_2/RuO_2 supercapacitor operating at 1.6 V by using a neutral aqueous electrolyte. Electrochem Solid-State Lett 15:A60–A63. https://doi.org/10.1149/2.023204esl

Xiao W, Xia H, Fuh JYH, Lu L (2009) Growth of single-crystal-MnO_2 nanotubes prepared by a hydrothermal route and their electrochemical properties. J Power Sources 193:935–938. https://doi.org/10.1016/j.jpowsour.2009.03.073

Xiong C, Aliev AE, Gnade B, Balkus KJ (2008) Fabrication of silver vanadium oxide and V_2O_5 nanowires for electrochromics. ACS Nano 2:293–301. https://doi.org/10.1021/nn700261c

Xu HY, Le XS, Li XD et al (2006) Chemical bath deposition of hausmannite Mn_3O_4 thin films. Appl Surf Sci 252:4091–4096. https://doi.org/10.1016/j.apsusc.2005.06.011

Xu M, Kong L, Zhou W, Li H (2007) Hydrothermal synthesis and pseudocapacitance properties of Î±-MnO_2 hollow spheres and hollow urchins. J Phys Chem C 111:19141–19147

Xu L, Ding Y, Chen C, Zhao L (2008) 3D flowerlike α-nickel hydroxide with enhanced electrochemical activity synthesized by microwave-assisted hydrothermal method. Chem Mater 20:308–316. https://doi.org/10.1021/cm702207w

Yan D, Cheng S, Zhuo RF et al (2009) Nanoparticles and 3D sponge-like porous networks of manganese oxides and their microwave absorption properties. Nanotechnology 20:105706–105717. https://doi.org/10.1088/0957-4484/20/10/105706

Yan J, Khoo E, Sumboja A, Lee PS (2010) Facile coating of manganese oxide on tin oxide nanowires with high-performance capacitive behavior. ACS Nano 4:4247–4255. https://doi.org/10.1021/nn100592d

Yan Y, Li B, Guo W et al (2016) Vanadium based materials as electrode materials for high performance supercapacitors. J Power Sources 329:148–169. https://doi.org/10.1016/J.JPOWSOUR.2016.08.039

Yang J, Li X, Bai SL et al (2011a) Electrodeposition and electrocatalytic characteristics of porous crystalline SnO_2 thin film using butyl-rhodamine B as a structure-directing agent. Thin Solid Films 519:6241–6245. https://doi.org/10.1016/J.TSF.2011.03.119

Yang Y, Kim D, Yang M, Schmuki P (2011b) Vertically aligned mixed V_2O_5–TiO_2 nanotube arrays for supercapacitor applications. Chem Commun 47:7746. https://doi.org/10.1039/c1cc11811k

Yang J, Lan T, Liu J et al (2013) Supercapacitor electrode of hollow spherical V_2O_5 with a high pseudocapacitance in aqueous solution. Electrochim Acta 105:489–495. https://doi.org/10.1016/J.ELECTACTA.2013.05.023

Yang P, Ding Y, Lin Z et al (2014) Low-cost high-performance solid-state asymmetric supercapacitors based on MnO2 nanowires and Fe_2O_3 nanotubes. Nano Lett 14:731–736. https://doi.org/10.1021/nl404008e

Yang F, Zhao M, Sun Q, Qiao Y (2015) A novel hydrothermal synthesis and characterisation of porous Mn_3O_4 for supercapacitors with high rate capability. RSC Adv 5:9843–9847. https://doi.org/10.1039/C4RA10175H

Yıldırım MA, Akaltun Y, Ateş A (2012) Characteristics of SnO_2 thin films prepared by SILAR. Solid State Sci 14:1282–1288. https://doi.org/10.1016/J.SOLIDSTATESCIENCES.2012.07.012

Yin AX, Liu WC, Ke J et al (2012) Ru nanocrystals with shape-dependent surface-enhanced raman spectra and catalytic properties: controlled synthesis and DFT calculations. J Am Chem Soc 134:20479–20489. https://doi.org/10.1021/ja3090934

Yin B, Zhang S, Yang J et al (2014) Facile synthesis of ultralong MnO_2 nanowires as high performance supercapacitor electrodes and photocatalysts with enhanced photocatalytic activities. CrystEngComm 16:9999–10005. https://doi.org/10.1039/C4CE01302F

Yu C, Zhang L, Shi J et al (2008) A simple template-free strategy to synthesize nanoporous manganese and nickel oxides with narrow pore size distribution, and their electrochemical properties. Adv Funct Mater 18:1544–1554. https://doi.org/10.1002/adfm.200701052

Yu D, Chen C, Xie S et al (2011) Mesoporous vanadium pentoxide nanofibers with significantly enhanced Li-ion storage properties by electrospinning. Energy Environ Sci 4:858–861. https://doi.org/10.1039/C0EE00313A

Yu M, Liu X, Wang Y et al (2012) Gas sensing properties of p-type semiconducting vanadium oxide nanotubes. Appl Surf Sci 258:9554–9558. https://doi.org/10.1016/J.APSUSC.2012.05.120

Yu A, Chabot V, Zhang J (2013a) Electrochemical supercapacitors for energy storage and delivery: fundamentals and applications. CRC Press

Yu Z, Duong B, Abbitt D, Thomas J (2013b) Highly ordered MnO_2 nanopillars for enhanced supercapacitor performance. Adv Mater 25:3302–3306. https://doi.org/10.1002/adma.201300572

Yu M, Zeng Y, Han Y et al (2015) Valence-optimized vanadium oxide supercapacitor electrodes exhibit ultrahigh capacitance and super-long cyclic durability of 100 000 cycles. Adv Funct Mater 25:3534–3540. https://doi.org/10.1002/adfm.201501342

Yuan L, Xiao X, Ding T et al (2012) Paper-based supercapacitors for self-powered nanosystems. Angew Chem Int Ed 51:4934–4938. https://doi.org/10.1002/anie.201109142

Zhang LL, Wei T, Wang W, Zhao XS (2009) Manganese oxide – carbon composite as supercapacitor electrode materials. Microporous Mesoporous Mater 123:260–267

Zhang Z, Zou R, Song G et al (2011) Highly aligned SnO_2 nanorods on graphene sheets for gas sensors. J Mater Chem 21:17360. https://doi.org/10.1039/c1jm12987b

Zhang X, Cheng X, Zhang Q (2016a) Nanostructured energy materials for electrochemical energy conversion and storage: a review. J Energy Chem 25:967–984. https://doi.org/10.1016/j.jechem.2016.11.003

Zhang Y, Zheng J, Zhao Y et al (2016b) Fabrication of V_2O_5 with various morphologies for high-performance electrochemical capacitor. Appl Surf Sci 377:385–393. https://doi.org/10.1016/J.APSUSC.2016.03.180

Zhao X, Johnston C, Grant PS (2009) A novel hybrid supercapacitor with a carbon nanotube cathode and an iron oxide/carbon nanotube composite anode. J Mater Chem 19:8755. https://doi.org/10.1039/b909779a

Zheng JP, Cygan PJ, Jow TR (1995) Hydrous ruthenium oxide as an electrode material for electrochemical capacitors. J Electrochem Soc 142:2699–2703

Zheng F-L, Li G-R, Ou Y-N et al (2010) Synthesis of hierarchical rippled Bi_2O_3 nanobelts for supercapacitor applications. Chem Commun 46:5021. https://doi.org/10.1039/c002126a

Zheng H, Ou JZ, Strano MS et al (2011) Nanostructured tungsten oxide – properties, synthesis, and applications. Adv Funct Mater 21:2175–2196. https://doi.org/10.1002/adfm.201002477

Zheng ZQ, Zhu LF, Wang B (2015) In_2O_3 nanotower hydrogen gas sensors based on both schottky junction and thermoelectronic emission. Nanoscale Res Lett 10:293. https://doi.org/10.1186/s11671-015-1002-4

Zheng W, Zhang P, Tian W et al (2017) Microwave-assisted synthesis of SnO_2-Ti_3C_2 nanocomposite for enhanced supercapacitive performance. Mater Lett 209:122–125. https://doi.org/10.1016/J.MATLET.2017.07.131

Zhong C, Deng Y, Hu W et al (2015) A review of electrolyte materials and compositions for electrochemical supercapacitors. Chem Soc Rev 44:7484–7539. https://doi.org/10.1039/c5cs00303b

Zhou T, Mo S, Zhou S et al (2011) Mn_3O_4/worm-like mesoporous carbon synthesized via a microwave method for supercapacitors. J Mater Sci 46:3337–3342. https://doi.org/10.1007/s10853-010-5221-x

Zhou G, Wang D-W, Hou P-X et al (2012) A nanosized Fe_2O_3 decorated single-walled carbon nanotube membrane as a high-performance flexible anode for lithium ion batteries. J Mater Chem 22:17942. https://doi.org/10.1039/c2jm32893c

Zhu J, Cao L, Wu Y et al (2013) Building 3D structures of vanadium pentoxide nanosheets and application as electrodes in supercapacitors. Nano Lett 13:5408–5413. https://doi.org/10.1021/nl402969r